

**A COMPARISON OF THREE COMPUTATIONAL
PHANTOMS FOR CALIBRATION OF A RADIATION
PORTAL MONITOR USED FOR MEASUREMENT OF
INTERNAL CONTAMINATION**

by

Christopher Bellman

A Thesis Submitted in Partial Fulfillment
of the Requirements for the Degree of

Master of Applied Science in Nuclear Engineering

In

The Faculty of Energy Systems and Nuclear Engineering Graduate Program

University of Ontario Institute of Technology

December 2014

©Christopher Bellman (2014)

ABSTRACT

The goal of this research was to investigate if portal monitors could measure internally deposited radioisotopes over a short count time (1 second) with a detection limit sufficient to measure 1/10 of an annual limit on intake (ALI) of specific radionuclides. The goal was to determine if portal monitors in nuclear facilities were able to effectively screen workers for internal contamination knowing the counting efficiencies for measuring internally deposited radioisotopes is poorer than measuring the same activity of external contamination and that intakes of radioisotopes result in a committed lifetime dose that is greater than the dose expected from external contamination.

This research investigated the counting efficiency of the Thermo PM12 personnel portal monitor for the measurement of internal contamination localized to the lungs. A counting efficiency curve was calculated by Monte Carlo analysis using Monte Carlo N Particle (MCNP) software. The counting efficiencies were used to calculate the minimum detectable activity for ^{241}Am , ^{57}Co , ^{60}Co , ^{137}Cs and ^{40}K as a function of sample (personnel) measurement time.

Three different computational phantoms were considered for this work: the adult male Bottle Mannequin Absorber (BOMAB) phantom, the University of Florida – Oak Ridge National Laboratories (UF-ORNL) stylized phantom, and the International Commission on Radiological Protection (ICRP) adult male voxel phantom. A percent difference ranging from 10-15% and 25-30% was observed at high energies (100-2000 keV) for the UF-ORNL and voxel computational

phantoms respectively using the counting efficiency measurements calculated for the BOMAB as a baseline. At low energies (< 100 keV) the percent difference dropped 20% (e.g., 10% to -10%) within a span of 60 keV for both the UF-ORNL and ICRP computational phantoms.

The ICRP voxel and the UF-ORNL computational phantoms allowed for greater accuracy for the source distribution. The BOMAB computational phantom was limited in that the source distribution was limited to one or more bottles. The BOMAB phantom was necessary to compare physical measurements to simulated measurements to assess the validity of the PM12 computational model across a range of energies.

This work shows that the PM12, and other portal monitors of similar build, are able to achieve detection limits of 1/100 ALI for the beta/gamma radiation emitting radioisotopes assessed. In general, the PM12 was well suited to measure internally deposited radionuclides with gamma emissions greater than 100 keV and with an ALI greater than 10^5 Bq with a short measurement time. Applying this work to radioisotopes with gamma emissions below 100 keV or with low ALI values (less than 10^5 Bq), such as ^{241}Am should be done with caution.

Keywords: MCNP, phantom, voxel, stylized, BOMAB, Monte Carlo, internal contamination, portal monitor

ACKNOWLEDGEMENTS

I would like to acknowledge the University Networks of Excellence in Nuclear Engineering (UNENE) and the Natural Sciences and Engineering Research Council (NSERC) for their support provided through University of Ontario Institute of technology (UOIT)

I would like to thank the staff at the Health Canada (HC) Human Monitoring Laboratory (HML) for supporting my MCNP modeling and simulation efforts for this work. The MCNP expertise of Kevin was particularly appreciated.

I would also like to thank Dan at Ontario Power Generation (OPG) for providing me a warm welcome during my work at your laboratories.

I would like to thank my friends and family for their support and love. Megan, you kept me going during the entire process.

Most of all I would like to thank my supervisor Dr. Ed Waller for his support and patience. Thank you for pushing me to make the most of my research and education.

TABLE OF CONTENTS

ABSTRACT	ii
ACKNOWLEDGEMENTS	iv
TABLE OF CONTENTS	v
LIST OF FIGURES	vii
LIST OF TABLES.....	ix
LIST OF Acronyms.....	x
1. Introduction	1
2. Background	6
2.1 Application of phantoms for the calibration of measurement systems	6
2.2 Scintillator counting systems.....	11
2.3 Monte Carlo radiation transport	19
3. Study Parameters.....	23
3.1 Portal monitor	23
3.2 Computational phantoms.....	25
3.2.1 <i>Stylized phantoms</i>	26
3.2.2 <i>Voxel phantoms</i>	28
3.2.3 <i>BREP phantoms</i>	30
3.3 Selection of computational phantoms	33

3.4	Monte Carlo radiation transport software	36
3.5	Operational dose quantities	41
4.	Methodology	45
4.1	Overview	45
4.2	Development of the PM12 model.....	46
4.3	Performance of benchmarking measurements	46
4.3.1	<i>Background measurements</i>	47
4.3.2	<i>Button source measurements</i>	47
4.3.3	<i>Centroid efficiency measurements</i>	48
4.3.4	<i>BOMAB phantom measurements</i>	50
4.4	Performance of simulations for benchmarking data.....	53
4.4.1	<i>Centroid efficiency</i>	53
4.4.2	<i>BOMAB simulation</i>	54
4.5	Development of counting efficiency curves.....	55
4.6	Calculation of the detection limit	57
5.	Results and discussion	62
5.1	Development of the PM12 model.....	62
5.1.1	<i>Description and specifications of the PM12</i>	62
5.1.2	<i>Development of the PM12 model</i>	63
5.1.3	<i>Photon energy binning</i>	65
5.2	Benchmarking measurements and simulations	67
5.2.1	<i>Centroid efficiency benchmarking</i>	67
5.2.2	<i>BOMAB phantom benchmarking</i>	72

5.2.3	<i>Counting efficiency curve simulations</i>	73
5.3	Calculation of the detection limit	77
6.	Conclusions and reccomendations for future work	82
6.1	Conclusions	82
6.2	Recommendation for future work.....	83
	REFERENCES	85
Annex A.	BOMAB fill solution calibration report	94
Annex B.	Gamma ray emission energies and yields	95
Annex C.	Benchmarking measurements data	96
Annex D.	Simulation data	97
Annex E.	MCNP input card	100

LIST OF FIGURES

Figure 1:	Range of alpha particle in tissue [5].....	3
Figure 2:	Author's rendition of the Fisher-Snyder phantom.....	8
Figure 3:	The BRMD BOMAB series.....	10
Figure 4:	A typical scintillation counter set-up.....	12
Figure 5:	Gamma-ray spectrum of a Cs-137 source	13
Figure 6:	Methods to increase the counting efficiency of a counting system	15
Figure 7:	Energy levels of the π -electron structure of an organic scintillator [25] 17	
Figure 8:	Dominant photon interaction mechanisms as a function of photon energy and Z of the absorber	19

Figure 9: Thermo PM12 a) dimensions; b) crude representation of the PVT detector locations	24
Figure 10: PM 12 position of lead shielding	25
Figure 11: Interior features of the MIRD phantom.....	27
Figure 12: Zubal voxel phantom (skin, fat and bones highlighted)	29
Figure 13: A lung defined by the (a) CSG, (b) voxel and (c) BREP modeling techniques	30
Figure 14: A curved line represented using the NURBS method	31
Figure 15: One axial slice of the male Visible Human image set	32
Figure 16: NCAT phantom	32
Figure 17: Phantoms considered in this study	40
Figure 18: Methodology overview	45
Figure 19: Positioning of the button source on a PVT detector	48
Figure 20: Centroid efficiency measurements.....	49
Figure 21: BOMAB phantom measurements	50
Figure 22: Photon attenuation cross section for CH from XCOM.....	52
Figure 23: BOMAB computational phantom inside of the PM12 model	55
Figure 24: Plotting the source distribution for each computational phantom	57
Figure 25: Depiction of the decision level and detection limit.....	59
Figure 26: PM12 with housing removed.....	63
Figure 27: Model of the PM12.....	64
Figure 28: PM12 centroid efficiencies (simulated, measured and manufacturer)	68
Figure 29: Photon absorption coefficients for some common elements [25].....	72

Figure 30: Efficiency curves for three computational phantoms.....	75
Figure 31: Bias plots for three computational phantoms	75
Figure 32: Detection limit as a function of sample count time	78
Figure 33: MDA as a function of sample time	80
Figure 34: ALI as a function of sample time	81

LIST OF TABLES

Table 1: MCNP tally confidence intervals	21
Table 2: BOMAB phantom dimensions	40
Table 3: Dose limits for NEWs and the public.....	42
Table 4: Button source activities (adjusted to April 15, 2012)	47
Table 5: Activities of the BOMAB fill solution	53
Table 6: PM12 material composition.....	65
Table 7: Centroid efficiency benchmarking results	68
Table 8: Sources of error between measure and simulated centroid efficiencies	70
Table 9: BOMAB phantom benchmarking results	73
Table 10: Constants for detection limit measurements	77
Table 11: Detection limit as a function of sample time	78
Table 12: MDAs calculated as a function of sample time.....	79
Table 13: Annual Limits on Intake.....	80

LIST OF ACRONYMS

ALI	Annual limit on intake
BOMAB	Bottle Manikin Absorber
Bq	Becquerel
BREP	Boundary representation
CAD	Computer aided design
CNSC	Canadian Nuclear Safety Commission
cps	counts per second
CSG	Constructive solid geometry
CT	Computed tomography
ICRP	International Commission on Radiological Protection
LANL	Los Alamos National Laboratories
MCA	Multichannel analyzer
MCNP	Monte Carlo N Particle
MDA	Minimum detectable activity
MRI	Magnetic resonance imaging
NURBS	Non-uniform rational basis spline
OPG	Ontario Power Generation
ORNL	Oak Ridge National Laboratories
PMT	Photomultiplier tube
PVT	Polyvinyl toluene
UF-ORNL	University of Florida-Oak Ridge National Laboratories

1. INTRODUCTION

Personnel portal monitors (henceforth referred to as “portal monitors”) are used to rapidly monitor large groups of persons that have potentially become contaminated with radioactive material. One person walks through the portal monitor at a time to be monitored for contamination. Large volume scintillators are used to measure the gamma and sometimes beta radiation emitted from the contaminating material and the person is deemed to be not contaminated (clean) or contaminated (dirty) by comparison of the measurement signal to the background. An alarm will typically sound when a person is monitored and deemed to be dirty.

Portal monitors are used for applications requiring a large throughput of persons. Examples of this include contamination control at nuclear power plants and screening potentially contaminated persons resulting from a mass-contamination event.

Work performed by Kramer et. al. [1][2] have shown portal monitors to be highly sensitive for the measurement of gamma radiation, to the extent of requiring a large distance of separation between individual portal monitors being used to monitor potentially contaminated persons from a mass-contamination event. The work by Kramer used calibration point sources of activities up to the GigaBecquerel (GBq) range which is appropriate for contamination incidents such as that in Goiânia, Brazil [3] which involved the dispersion of a 74 TBq ^{137}Cs teletherapy source. Contamination events in a routine exposure context, for

example operations at a nuclear power plant, may result from the dispersion of much smaller activities.

Radioactive material that has entered the body through inhalation, ingestion or other means (internal contamination) is of particular concern. In comparison to external contamination, internal contamination will:

- a) Expose the individual until the radioactive material is cleared from the body via biological functions and/or radioactive decay (an exposure period ranging from hours to years depending on the radioisotope). External contamination exposes the individual until the contaminated clothing is removed and/or the contamination is washed off of the body (an exposure period of hours for operational exposures). Once radioactive material has been internalized, the resulting dose is calculated as a lifetime dose (50 years) from the intake – the committed effective dose or dose commitment [4];
- b) Possibly expose internal organs to highly energetic radiation with a very short range in tissue, such as alpha particles (approximately 3 μm for a 5 MeV alpha particle in tissue with a density of 1 g/cm^3 (Figure 1)), that would normally be absorbed by a person's clothing or dead layer of skin from an external contamination scenario; and
- c) Be more difficult to measure by a portal monitor system as gamma rays will be attenuated by the body. Portal monitors are designed with a focus on throughput, sometimes operating in a walk-through mode.

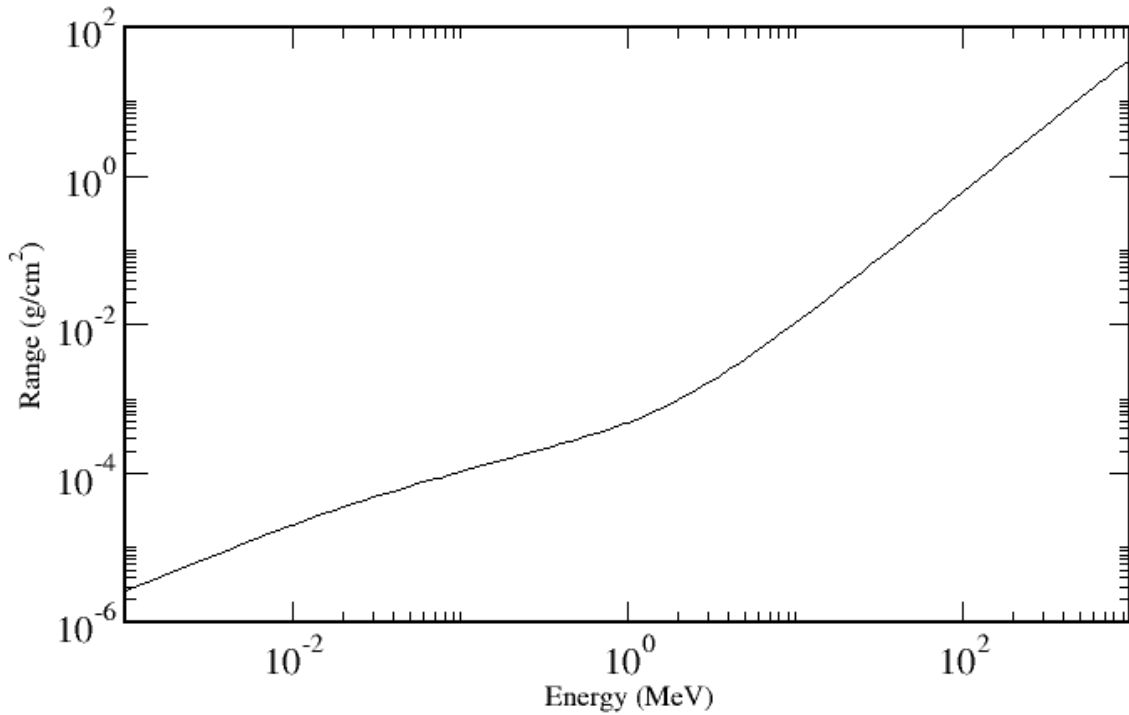


Figure 1: Range of alpha particle in tissue [5]

Based upon the above bullets, internal contamination will be more difficult to measure and will result in a greater dose when compared to the same activity of external contamination. The focus of this research is to determine if portal monitors are able to achieve detection limits acceptable to measure operationally significant activities of internal contamination in the context of the Canadian dose limits for nuclear energy workers (NEWs) [6]. The concept of operationally significant is discussed in Section 3.5. This necessitates the calculation of portal monitor calibration factors (cps/Bq) for measuring internally deposited radioisotopes.

The industry standard for the calibration of systems dedicated to the measurement of internal contamination, such as whole body counters, is the Bottle Mannequin Absorber (BOMAB) phantom [7]. A phantom is a model of the

whole or a part of a human body. The composition of the phantom is such that it approximates the density and elemental composition of bodily tissues. The BOMAB phantom is a physical model of the entire human body; it consists of ten elliptical and cylindrical bottles that are filled with a radioactive solution and assembled to approximate anthropomorphicity. Work performed by Kramer et. al. [8]-[10] has shown that whole body counters may also be calibrated with great precision by means of Monte Carlo analysis with computational models of the BOMAB phantom. Kramer also showed that the BOMAB phantom will provide a calibration uncertainty for whole body counters of up to 20% compared to the Normalized Man (NORMAN) phantom which more closely approximates anthropomorphicity [11]. NORMAN is a computational phantom developed by the United Kingdom Health Protection Agency using data from high resolution Magnetic Resonance Imaging (MRI) scans of a human body [12]-[13]. The MRI data was broken into 35 million 2 mm cubed voxels (cuboids); each voxel containing information on the density and elemental composition corresponding to the bodily tissue or organ containing the voxel.

Three computational phantoms were selected for the evaluation of the measurement efficiency of a portal monitor for internal contamination by Monte Carlo analysis: A computational model of adult male BOMAB phantom, a stylized computational phantom based upon the Medical Internal Radiation Dose (MIRD) phantom, and the International Commission on Radiological Protection (ICRP) voxel phantom of the reference man. These phantoms represent the external and internal features of the human body (anthropomorphicity) to different degrees

with the BOMAB being the poorest representation and the voxel phantom being the best. The effect of anthropomorphicity on the Monte Carlo analysis is investigated as a secondary focus of this research.

2. BACKGROUND

2.1 Application of phantoms for the calibration of measurement systems

Early computational phantoms were developed to support the assessment of doses to organs and bodily tissues from internally deposited radioactive materials (internal dose assessment). In the 1940's, internal dose assessments were performed using equations developed and presented by Marinelli and his colleagues [14]-[15]. These equations calculate the dose from both beta-emitting radioisotopes (considered non-penetrating radiation) using Equation 1 and from gamma rays (considered penetrating radiation) using Equation 2. Equation 1 was used under the assumption that the emitted beta radiation is completely absorbed by in the bodily tissue or organ of interest. A geometry factor (unitless) was applied for internal dose assessments for gamma-radiation to account for the radiation energy escaping the volume of interest.

$$D_{\beta} = 73.8E_{\beta}CT \quad \text{Equation 1}$$

$$D_{\gamma} = 0.0341CT\Gamma g \quad \text{Equation 2}$$

where

D_{β} is the absorbed dose from beta radiation (rad);

D_{γ} is the absorbed dose from gamma radiation (rad);

C is the radioisotope concentration ($\mu\text{Ci/g}$);

T is the effective half life of the radioisotope (day);

Γ is the specific gamma-ray constant for the radionuclide ($\text{R}/\mu\text{Ci-h}$); and

g is the geometry factor

In the 1960's work was performed to further refine the process for internal dose assessment. This saw the first introduction of computational phantoms. Reddey, Ellet, Callahan and Brownwell published the results of their Monte Carlo calculations for gamma-ray internal dosimetry [16]-[18]. They considered point and uniform volume distributed gamma-ray sources in computational organ phantoms represented by spheres, thick ellipsoids, flat ellipsoids, and elliptical cylinders. The computational phantoms were used to calculate the absorbed fraction in the organ [19]. The absorbed fraction is the ratio of the energy absorbed in a target organ or tissue over the total energy emitted by the radioactive material.

The next evolution of these simple phantoms was to develop a computational phantom representative of a human body. The first computational phantom of an adult male was developed at Oak Ridge National Laboratories by Fisher and Snyder [20]. The so-called Fisher-Snyder phantom was composed of only three specific regions: an elliptical cylinder to represent the head and neck, a separate elliptical cylinder to represent the trunk and arms, and a truncated cone to represent the legs (See Figure 2 for the author's rendition of the Fisher-Snyder phantom). A homogenous composition of tissue was assumed for the phantom. The phantom had approximately 120 sub-regions used to assign approximate values of absorbed doses to organs located within those regions.

The Fisher-Snyder phantom was used mainly to determine doses from internal sources of radiation; however it was also studied by Fisher and Snyder to determine doses from external sources [21].

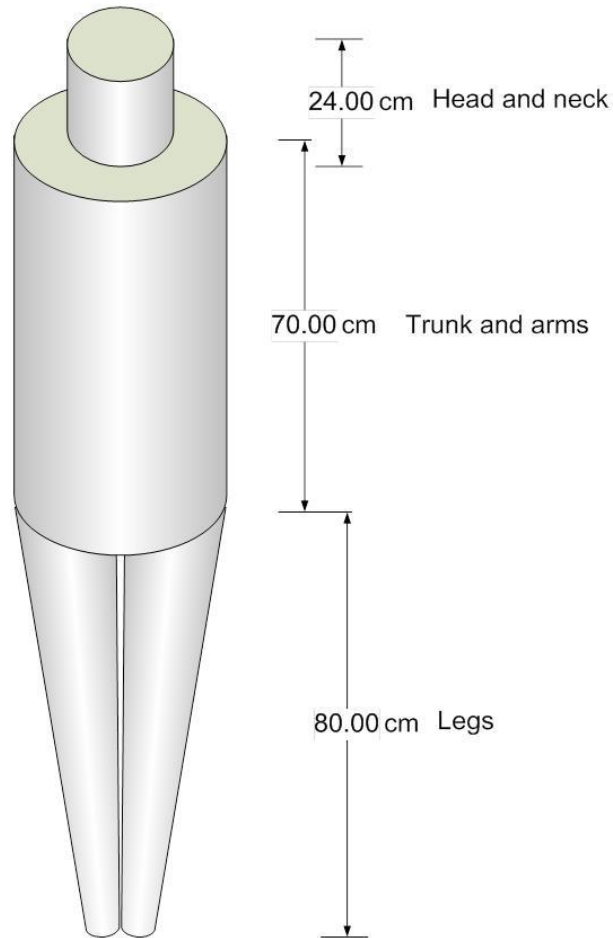


Figure 2: Author's rendition of the Fisher-Snyder phantom

These early computational phantoms were designed for the purpose of quantifying the radiation dose from internal and external sources. Other applications for phantoms arose as research in the field matured. One such application is the use of phantoms for the calibration of whole body counter (WBC) radiation counting systems designed to measure the body burden of internal sources.

The measurement of radiation using a system such as a whole body counter is a relative measurement. The measurement system must be calibrated to relate the measurement signal to a known activity of radioactive material. Calibration is performed by measuring a sample with a known activity composition and photopeak energy to develop a measurement efficiency (e.g. Bq/cps) at that energy. Numerous sources representing a variety of energies are often used to generate a calibration curve as a function of photopeak energy. For the specific case of the whole body counter, phantoms are used to calibrate the system as it is designed to measure the activity of contamination inside of the human body. The industry standard for calibration of whole body counters is the BOMAB phantom [7]. The original BOMAB phantom was designed by Bush in 1949 [22]. BOMAB phantoms representative of the reference male, female and children of age 10 and 4 years (Figure 3) representative of the reference body types described in ICRP 23 [24] were later developed [23].

Calibration is performed by filling the bottles with a known activity of a radioactive, gamma-emitting solution. The process is repeated with radioactive solutions containing different isotopes with gamma emissions spanning an energy range of approximately 60 keV to 3000 keV to develop an efficiency curve as a function of energy for the whole body counter.

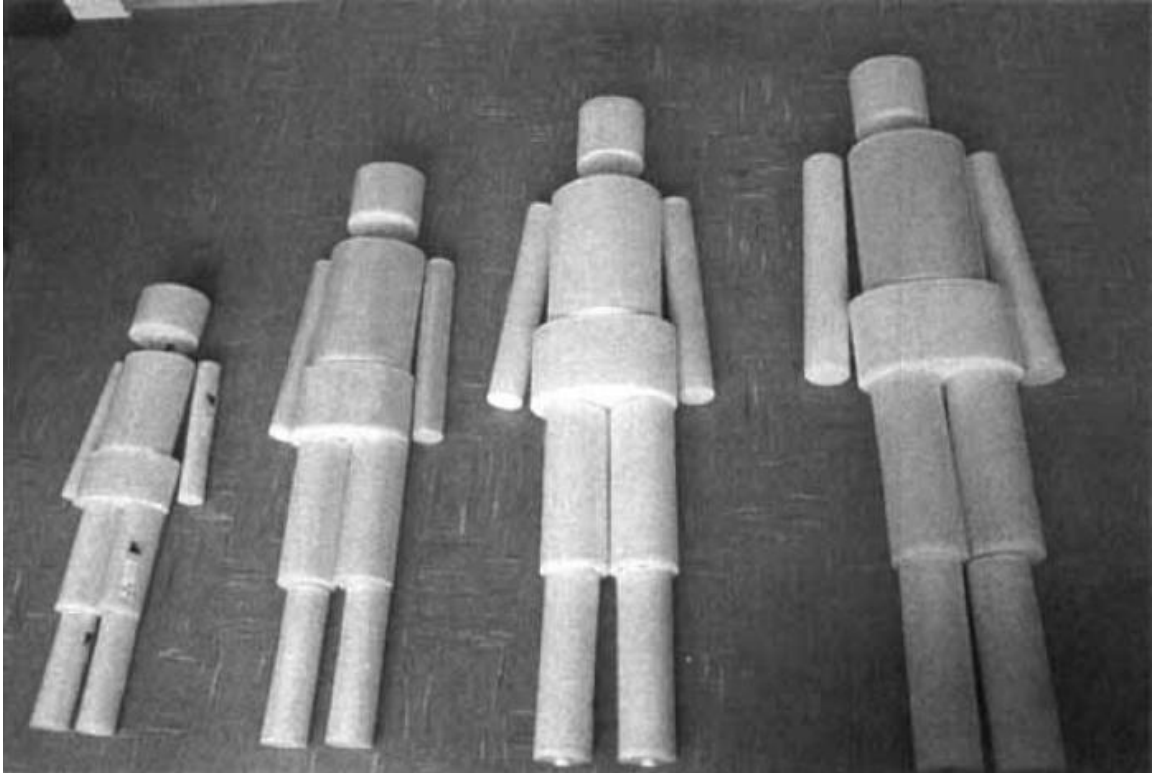


Figure 3: The BRMD BOMAB series

Computational phantoms have also been used to calibrate whole body counters. Kramer et al. calibrated various whole body counters using the Monte Carlo computational models of the BOMAB phantoms [8]-[10] with a computational model of a whole body counter. The transportation of gamma rays was simulated using the Monte Carlo radiation transport code entitled Monte Carlo N Particle (MCNP). The detector response was found to be calculated with good precision when a large number of particles were simulated.

Work performed by Kramer et al [76] has attempted to quantify the uncertainty in activity estimations from lung counting due to variations in patient chest wall thicknesses. Chest wall thicknesses were measured via ultrasound on eight male and fourteen female volunteers. Chest thickness was measured in

four areas corresponding to the upper and lower part of the left and right lung. No pictures of the chest wall thickness measurement geometries are provided.

The averaged chest wall thicknesses (average of the four measurements) for males ranged from 2.5 to 4.0 cm with a mean of 3.2 cm and standard deviation of 0.55 cm. The averaged chest wall thicknesses for females ranged from 2.0 to 5.0 cm with a mean of 3.3 cm and standard deviation of 0.92 cm. On average, the female chest wall thickness is greater than the male due to the effect of breast size.

The counting efficiency of the lung counter was evaluated using MCNP4. The chest wall thickness of the chest phantom computational model was altered to correspond to the measured chest wall thicknesses from the patients. The uncertainty on the estimation of activity due to chest wall thickness was determined to be an over or underestimate of about a factor of 1.07. In some extreme cases for females the factor may be about 1.2.

2.2 Scintillator counting systems

Some materials will scintillate (emit visible light) when they have absorbed energy from incident ionizing radiation. These materials can be coupled with instrumentation to convert the light pulse into an electric signal that may be used to count the number of radiation particles that interact with the scintillator material over a period of time. The visible light yield is proportional to the energy deposited by the radiation particle over a wide range of energy for a good scintillator material. Thus, the intensity of the measured electrical pulse can be used to determine the energy of the incident particle.

A typical set-up for a scintillation counting system is shown in Figure 4

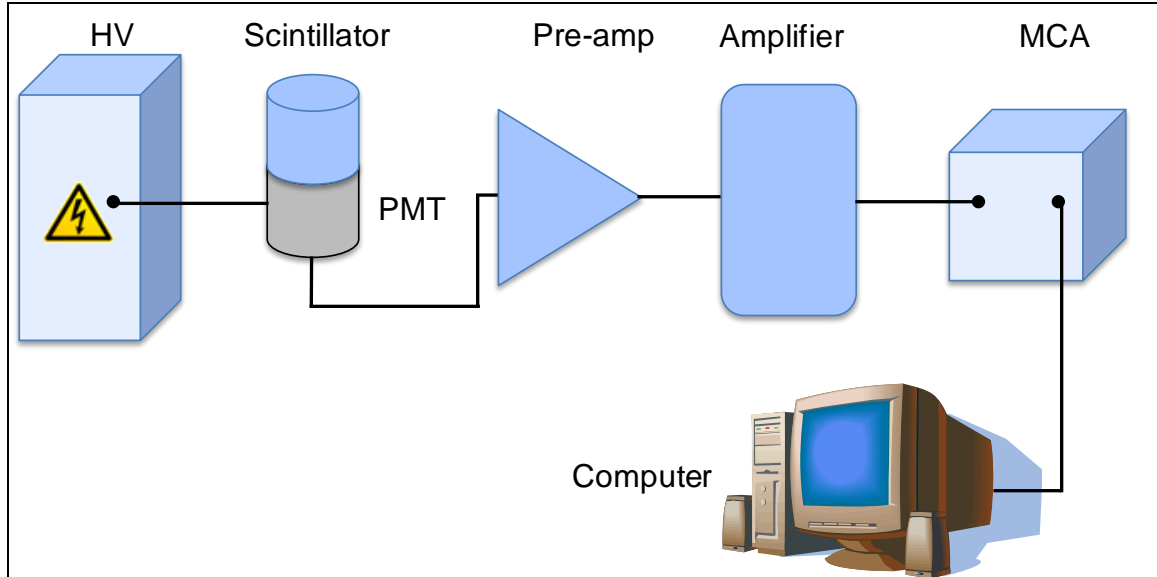


Figure 4: A typical scintillation counter set-up

where

HV is the high voltage power supply to the photomultiplier tube;

PMT is the photomultiplier tube used to convert the light photons from the scintillator into an electrical pulse;

Pre-amp is the preamplifier used to convert the low-amplitude, short duration pulse from the PMT into a voltage pulse with amplitude proportional to the energy deposited in the scintillator;

Amplifier amplifies and shapes the pulse to meet the input requirements of the multichannel analyzer;

MCA is the multichannel analyzer that will bin the electrical pulse based upon its height; and

The *computer* allows the user to view the spectrum generated by the MCA using an appropriate software. The spectrum is output with axes of counts/channel. If the energy calibration of the counting system is known the software will calculate the energy value of the spectrum channels.

The output of the depicted system for the measurement of a Cs-137 source may resemble Figure 5. The amplitude of the scintillation light is proportional to the electrical pulse and the respective binning. The observable peak, called the photopeak, in the 190-240 channel range is due to the 663 keV gamma-ray emission from Cs-137.

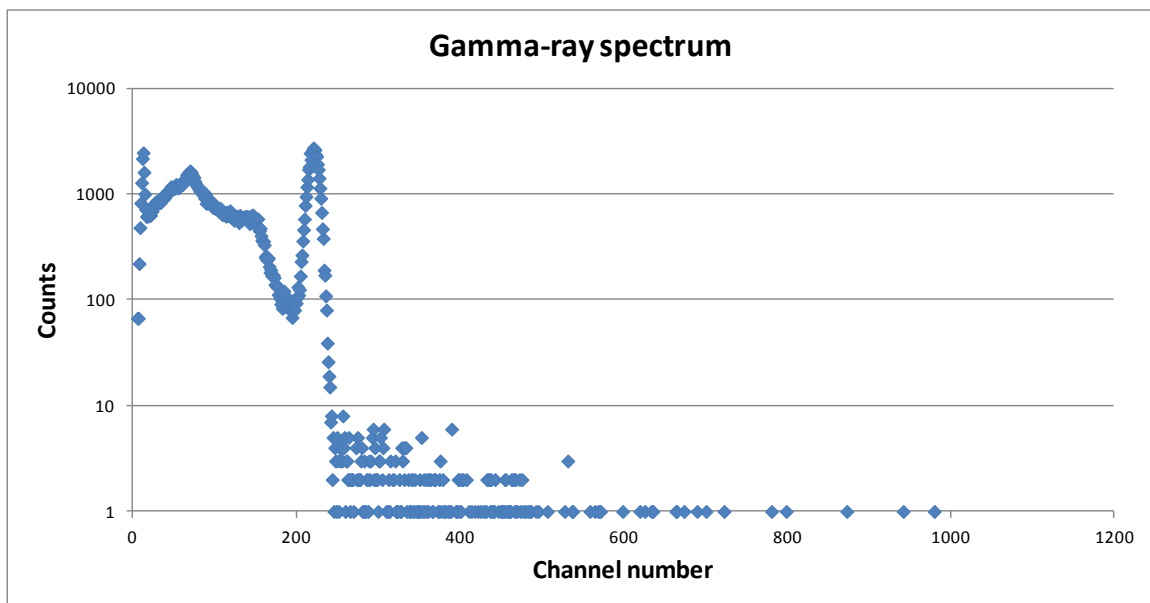


Figure 5: Gamma-ray spectrum of a Cs-137 source

The efficiency of the radiation counting system is calculated using Equation 3. The counting efficiency is measured over a fixed sample time or it may also be integrated for time and solved as a count rate. For the specific case of whole body monitor and portal monitors, the counting efficiency is measured for gamma-radiation only.

$$\varepsilon = \frac{N_m}{T \times A \times \sum_i BR_i} \quad \text{Equation 3}$$

where

ε is the counting efficiency (counts/photon);

N_m is the total number of measured radiation particles (counts); and

T is the sample time (seconds);

A is the activity of the measured source (disintegrations/second); and

BR_i is the branching ratio for photon i emitted from the radioisotope (photon/decay).

Referring back to Figure 5, the net counts in the 663 keV photopeak may be calculated by integrating the total number of counts under the photopeak and subtracting the number of background counts in the same channels. Solving Equation 3 will yield the counting efficiency at the specific energy for that photopeak – 663 keV in this case. Repeating this process for one radioisotope or a mixture of radioisotopes that span a wide range of gamma-ray emission energies will yield a counting efficiency curve.

There are several methods for increasing the counting efficiency of a counting system (depicted in Figure 6), assuming that the characteristics of the source cannot be changed:

- a) Decrease the distance from the source to the detector (d_o to d_i);
- b) Increase the volume of the detector (r_o to r_i); and
- c) Select a detector with superior photon interaction cross sections

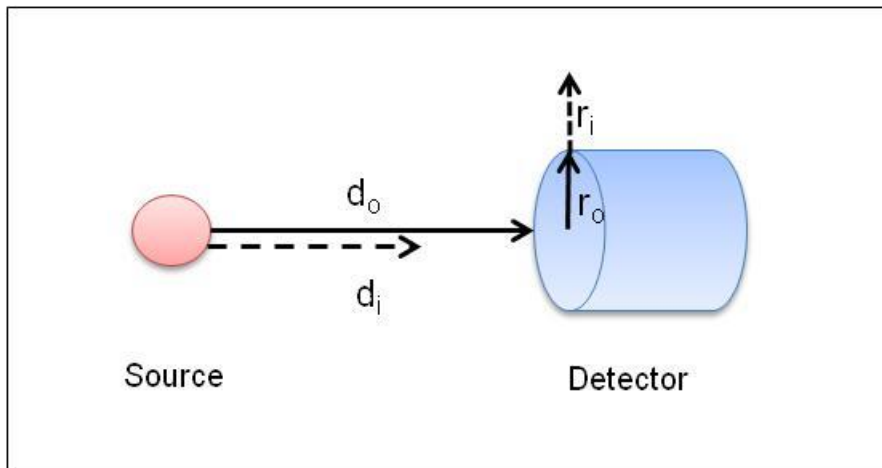


Figure 6: Methods to increase the counting efficiency of a counting system

The counting efficiency is a primary concern for radiation portal monitors. Superior counting efficiencies allow for shorter counting times to measure the same number of counts from a source. A shorter counting time allows for higher throughput of workers.

Most radiation portal monitors make use of plastic scintillator detectors which can be manufactured in large volumes for relatively low costs. Plastic scintillators are a sub-category of the organic scintillator family. The scintillation process for organic scintillators, which may be broken into absorption, fluorescence (prompt emission of visible light), and phosphorescence (emission

of longer wavelength light than fluorescence with a characteristic time that is generally much slower), is described by Knoll in his text on Radiation Detection and Measurement [25].

Organic molecules with certain symmetry properties give rise to what is known as a π -electron structure. One such property is a benzene ring which is characterized by the delocalization of three π -bonds within the ring structure. The π -bonds give rise to a cloud of electrons above and below the molecular plane. The organic scintillator molecules are held together by van der Waals forces instead existing in a well ordered crystal matrix and bound together with covalent bonds [27].

A number of excited states exist in the π -electron structure and are shown in Figure 7. Singlet states (spin 0) are labeled as $S_0, S_1, S_2...$ and a similar set of triplet states (spin 1) are labeled as $T_1, T_2, T_3...$ Energy is absorbed from nearby passing charged particles transitioning the molecule to a higher energy state. The principal scintillation light (fluorescence) is emitted from de-excitation in the singlet energy states. Some excited singlet states may be converted to triplet states through a transition called intersystem crossing. The lifetime of the triplet energy states is longer than the singlet states, thus visible light emitted from de-excitation in these states is delayed (phosphorescence).

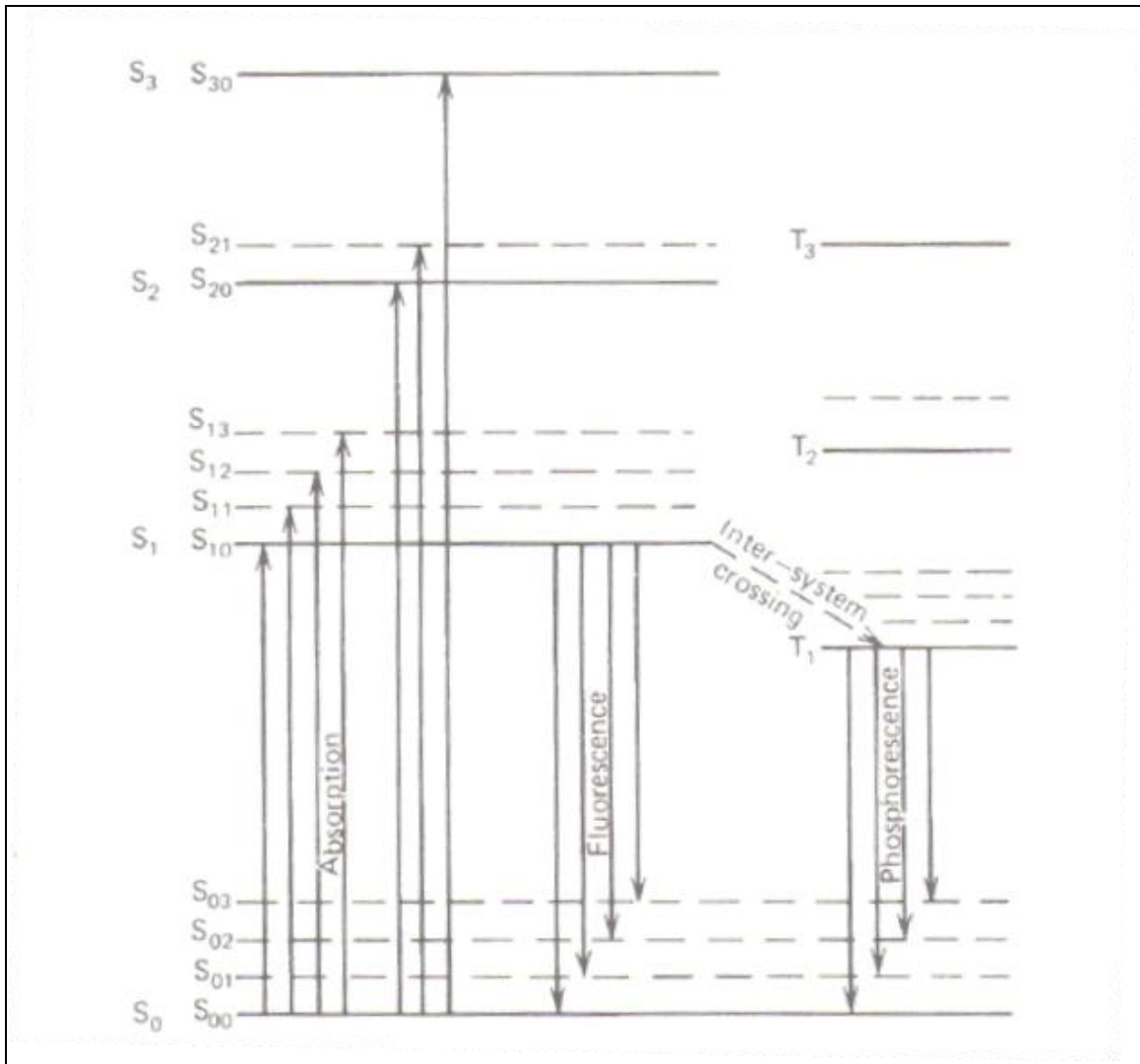


Figure 7: Energy levels of the π -electron structure of an organic scintillator [25]

Plastic scintillators suffer from two phenomena that will affect its performance as a scintillator: the photon absorption cross section for organic materials (carbon and hydrogen) is poor, thus photon scattering is the dominant interaction; and self-absorption of the scintillation light in large volume scintillators may not be negligible.

Figure 8 from Evans [26] depicts the dominant photon interactions as a function of the photon energy and the atomic number (Z) of the absorber. The photoelectric effect is the complete transfer of the photon energy to an orbital electron in the absorbing material; the photon disappears. The Compton effect is the transfer of a portion of the photon energy to an orbital electron depending on the scattering angle. Pair production is the complete absorption of the photon in the nucleus of the atom leading to the creation of an electron and positron; the positron will subsequently annihilate with an electron leading to the creation of two 511 keV photons emitted in opposite directions.

The elemental constituents of plastic are carbon and hydrogen. The atomic number for carbon and hydrogen are six and one, respectively. According to the Figure 8, the dominant photon mechanism at photon energies in the 0.1 to 2 MeV range (common gamma-ray emission energies for man-made radioisotopes) for these elements is the Compton effect. Since the Compton effect is dominant in organic scintillators, the production of gamma-ray spectra using fine-energy binning (e.g., 1024 or more bins) may not result in a gamma-ray spectrum as depicted in Figure 5 with an observable photopeak.

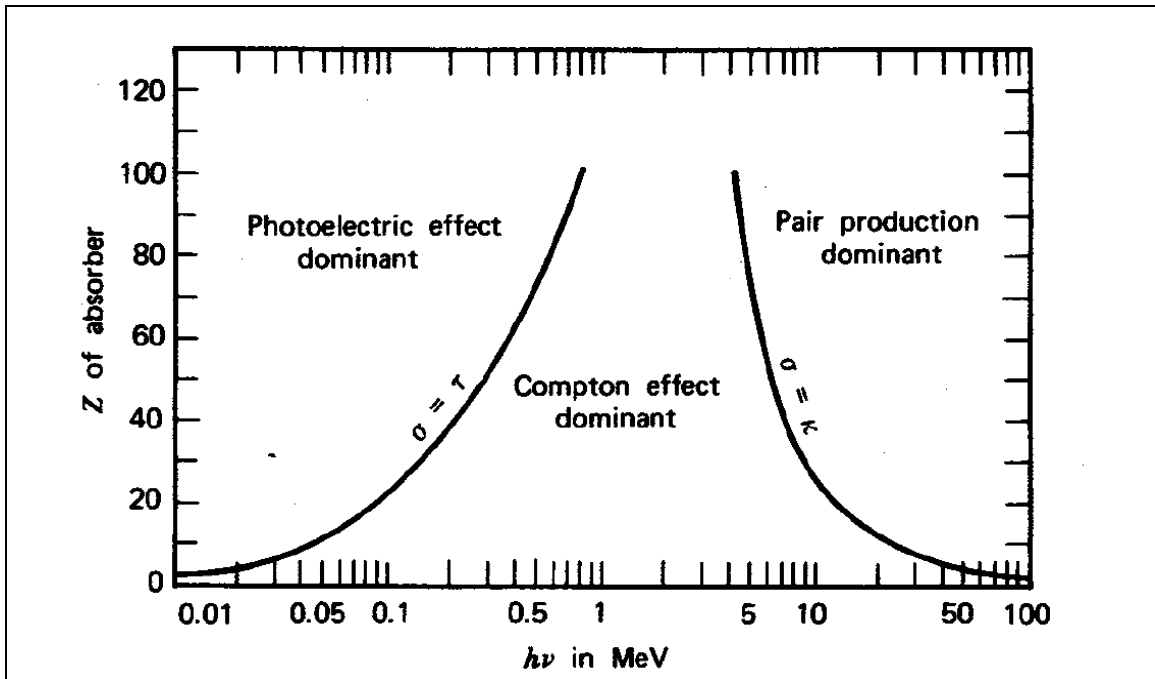


Figure 8: Dominant photon interaction mechanisms as a function of photon energy and Z of the absorber

As stated by Knoll, plastic scintillators are often the only practical choice if large-volume solid scintillators are needed. In these cases the self-absorption of the scintillator light may no longer be negligible, and some attention should be given to the attenuation properties of the material. This phenomenon may not be captured by Monte Carlo radiation transport codes and could lead to discrepancies between measured and simulated results.

2.3 Monte Carlo radiation transport

The Monte Carlo radiation transport code Monte Carlo N Particle (MCNP) is used to evaluate the counting efficiency of a radiation portal monitor system using Monte Carlo processes. MCNP was selected from a number of other Monte Carlo software, as described in Section 3.4. This section provides the relevant information about the application and limitations of MCNP.

MCNP is a general-purpose Monte Carlo radiation transport code that allows for coupled neutron/photon/electron simulations. MCNP obtains answers by simulating the transport of individual particles through a user-defined geometry. The User may request MCNP to provide information (tallies) on particle interactions or fluxes in specific areas of the geometry – a detector, for example. The average behaviour of particles in the physical system is then inferred using central limit theorem from the average behaviour of the simulated particles [28].

The radiation transport process is based upon randomly sampling numbers from probability distributions. The path of an individual particle is tracked from the source until the particle is killed due to pre-defined criteria (absorption, escape, etc.). This process is repeated for many particles. According to central limit theorem, the arithmetic mean of a sufficiently large number of iterations will be approximately normally distributed. Thus, for an appropriate number of particle histories, the answer provided by MCNP will converge upon the arithmetic mean of the expected physical phenomenon.

MCNP uses continuous energy nuclear and atomic libraries. The primary sources of nuclear data are evaluations from the Evaluated Nuclear Data File (ENDF) system, Advanced Computational Technology Initiative (ACTI), the Evaluated Nuclear Data Library (ENDL), Evaluated Photon Data Library (EPDL), the Activation Library (ACTL) compilations from Livermore, and evaluations for the Nuclear Physics (T-16) Group at Los Alamos.

The work for this research is only concerned with photon interactions and, as such, MCNP was run in photon mode. Photon interaction tables exist for all elements from $Z=1$ through $Z=100$ in MCNP. The data in the photon interaction tables allow MCNP to account for coherent and incoherent scattering, photoelectric absorption with the possibility of fluorescent emission, and pair production.

One of the underlying messages stated in the MCNP user manual [28] is for users to question the stability and reliability of results. MCNP is not able to compare simulated results with a physical system, but it does provide tools to ascertain the reliability of the tallies provided by the code. Each tally is accompanied with the estimated relative error of the tally, denoted as R . R is equal to one estimated standard deviation of the mean divided by the mean.

The relative error can be used to form confidence intervals of the estimated mean. The MCNP user's manual provides a guideline for interpreting the quality of the confidence interval for various values of R ; these are repeated in Table 1. Note that the confidence statement only refers to the precision of the Monte Carlo calculation itself and not the accuracy of the result compared to the true physical value.

Table 1: MCNP tally confidence intervals

Range of R	Quality of the tally
0.5 to 1.0	Not meaningful
0.2 to 0.5	Factor of a few
0.1 to 0.2	Questionable
< 0.1	Generally reliable
< 0.05	Reliable for point detectors

The accuracy of the MCNP model of the physical system can be verified by performing radiation counting measurements of an identical simulated geometry; referred to as benchmarking. Kramer and colleagues demonstrated the benchmarking process with a physical torso phantom obtained from Lawrence Livermore National Laboratory [29]. Kramer developed a computational phantom model from the LLNL torso phantom from a CT scan image set of the phantom. Scans were taken at a slice resolution of 5 mm and a second scan was performed at a resolution of 1.25 mm.

Measurements of the physical phantom were taken with a lung counting system consisting of 4 P-type germanium detectors. A model of the measurement geometry was created using MCNP and photon transport simulations were performed to evaluate the counting efficiency. The percent difference between the measured and simulated efficiencies were calculated and presented for seven different photon energies between the energy range of 17.5 and 344 keV. The simulated efficiencies were within 2 % of the measured efficiencies for the energy range of 59.5 to 344 keV. Below 59.5 keV the percent difference increased to a maximum of 57.9% at 17.5 keV.

The benchmarking process published by Kramer demonstrates the importance of comparing simulated and measured counting efficiencies. This shows the limitations of the model – which in this case were energy dependant.

3. STUDY PARAMETERS

3.1 Portal monitor

The portal monitor selected for this research was the model PM12 designed and manufactured by Thermo Fisher Scientific (Figure 9). Access was needed to a physical portal monitor to support modeling efforts and to perform benchmarking experiments. Thus, the main selection criterion for the portal monitor was availability.

Ontario Power Generation (OPG) utilizes a PM12 at their campus located in Whitby, ON. OPG made the PM12 available for inspection and benchmarking measurements.

The PM12 (Figure 9) contains eight polyvinyl toluene (PVT) plastic scintillators for the measurement of radiation. The PVT scintillators are arranged such that three are contained in each jamb and one each are contained in the ceiling and floor of the PM12 (Figure 9 b)). Light pulses in a PVT scintillator are measured by a photomultiplier tube (PMT). The PVT scintillators are 5 cm thick with an area of 31 cm by 56 cm. The PVT is a phosphor type BC408 manufactured by Bicron [72] wrapped in a foil, plastic and an aluminum jacket. One photomultiplier tube (PMT) is embedded in each PVT scintillator. The foil jacket is used to reflect scintillation light back to the PMT for counting purposes.

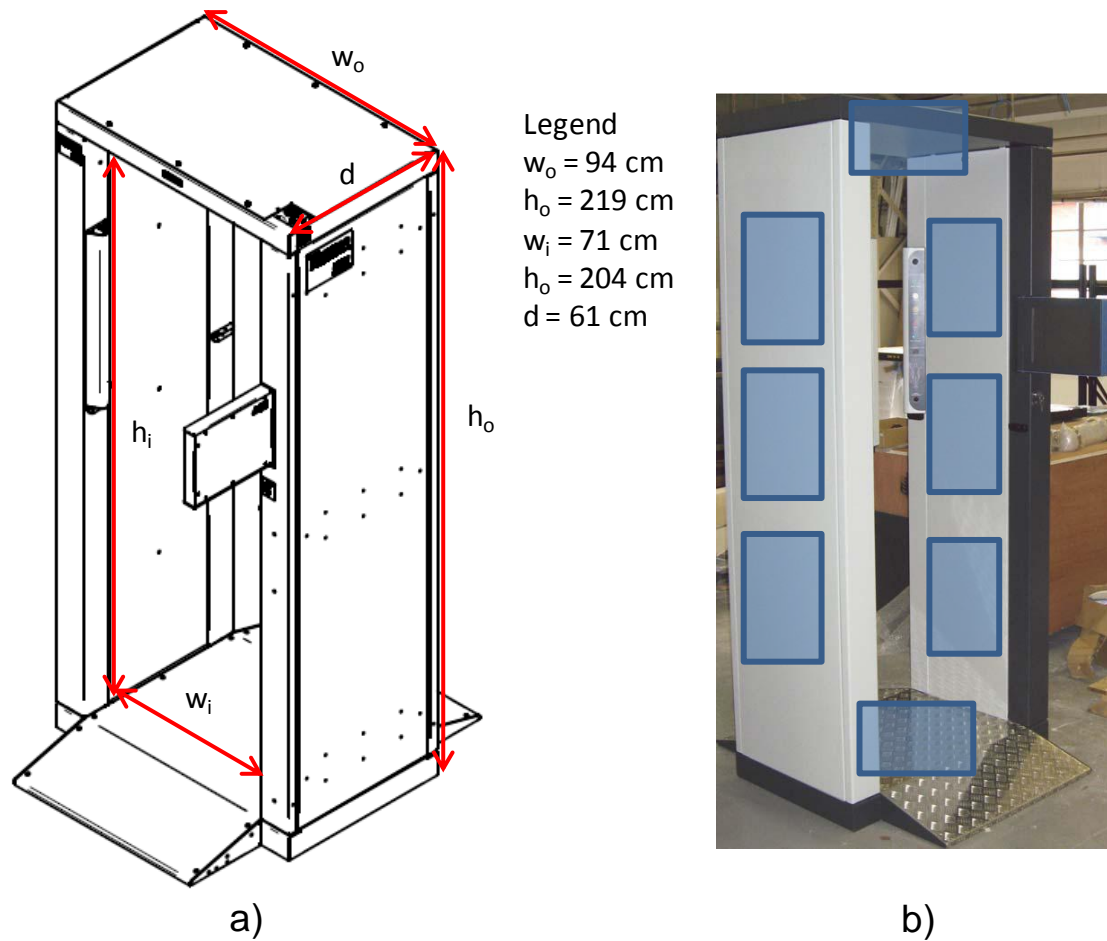


Figure 9: Thermo PM12 a) dimensions; b) crude representation of the PVT detector locations

The PVT scintillators are shielded by 1.25 cm of lead. The lead is used to reduce noise from background sources of radiation. The lead shielding is located between the PVT detector and the PM12 housing as depicted in Figure 10.

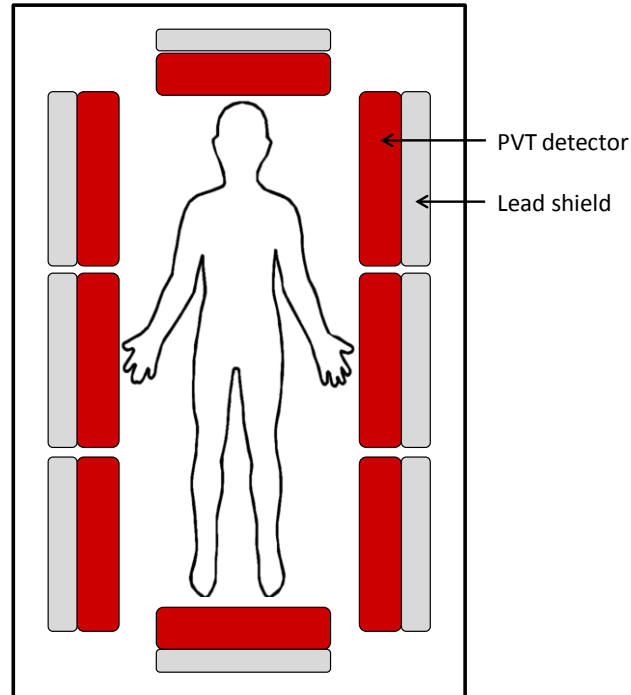


Figure 10: PM 12 position of lead shielding

The PVT scintillators, lead shielding and other electronic components are contained in a housing. The housing consists of aluminum covers for the jambs, an aluminum floor plate and a steel lid/ceiling. Refer to Figure 9 for the dimensions of the PM12 housing.

3.2 Computational phantoms

The Handbook of Anatomical Models for Radiation Dosimetry (Xu and Eckerman) [19] provides a history of the developments of computational phantoms. Xu and Eckerman have performed a review of scientific literature relating to the computational phantoms developed by the scientific community for Monte Carlo analysis. The results of their literature review are not repeated in this thesis; however the phantoms presented in their review were considered in the selection of the phantoms for this research.

Xu and Eckerman categorize computational phantoms into three classes: stylized phantoms, voxel phantoms and boundary representation (BREP) phantoms. The three classes of phantoms are described in the following sections.

3.2.1 Stylized phantoms

Stylized phantoms are developed using constructive solid geometry (CSG) modeling techniques. CSG allows modelers to create a solid object using Boolean operators to combine very simple objects such as cylinders, spheres, cones and ellipsoids. These simple objects are created using surfaces that are easily described by quadratic equations.

The earliest stylized phantoms were simple shapes: spheres, disks and cylinders. The phantoms were assumed to be composed of water to simplify the dosimetry calculations. These phantoms were used from 1964 to 1967 to estimate the absorbed fraction of energy in the phantom from photon irradiations. The specific absorbed fraction is the fraction of energy from an emitted radiation absorbed in a specific target tissue. The results of the work with these phantoms were published in the Medical Internal Radiation Dose (MIRD) pamphlets [34].

The earliest stylized phantom that approximated anthropomorphicity was the Fisher-Snyder phantom developed at Oak Ridge National Laboratories (ORNL). The phantom is described in Chapter 2 of this thesis. In short, it was defined by three regions, the head and neck, the trunk and arms, and the legs. The phantom was assumed to be tissue equivalent throughout.

The work by Fisher and Snyder led to the development of a heterogeneous phantom consisting of three regions: skeleton, lungs and the remainder (approximated as soft tissue) [37]-[38]. These regions had separate densities of approximately 1.5, 0.3 and 1.0 g/cm³ respectively. The organ masses were selected to follow the data of the ICRP reference man [24] as closely as possible. This phantom became known to the medical community as the “MIRD” phantom [19].

Figure 11 depicts the interior features of the MIRD phantom. The colouring of the internal organs is performed according to the material: lung (pink), bone (grey) and soft tissue (blue).

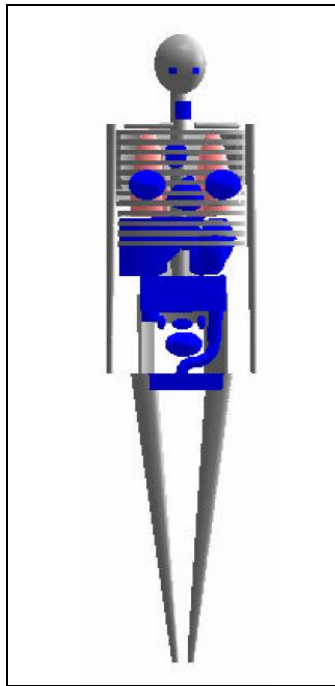


Figure 11: Interior features of the MIRD phantom

3.2.2 Voxel phantoms

With the advent of computed tomography (CT) and magnetic resonance imaging (MRI) techniques, researchers could visualize the internal structures of the body in three dimensions and store the images in versatile digital formats. These images from live patients and cadavers brought about the development of voxel phantoms. A voxel is simply a three dimensional representation of a pixel – a cuboid.

The tomographic image data set is composed of many slices, each displaying a two dimensional pixel map of the anatomy. The three dimensional volume of the voxel is measured by multiplying the pixel size by the thickness of the image slice. The voxel phantom contains a large number of tiny cuboids grouped to represent various anatomical structures.

The Zubal phantom developed at Yale University is one of the earliest voxel phantoms [39][40]. A patient at the Yale University hospital was scheduled for head, thorax, abdomen and pelvic CT scans for the diagnosis of diffuse melanoma. The patient was an ideal candidate for this work as his physical dimensions are similar to that of the MIRD mathematical phantom which was the standard for dosimetry calculations at the time [34]. The patient agreed to release his scan data for research purposes.

A total of 78 slice images were obtained from neck to mid-thigh with a 1 cm slice thickness. A further 51 slices of the neck and head region were obtained with a 5 mm slice thickness. A total of 35 organs and known internal structures were delineated by medical staff. Figure 12 depicts the Zubal phantom with the skin, fat and bones highlighted.

The Zubal phantom is still available for download on the Zubal phantom website [41].

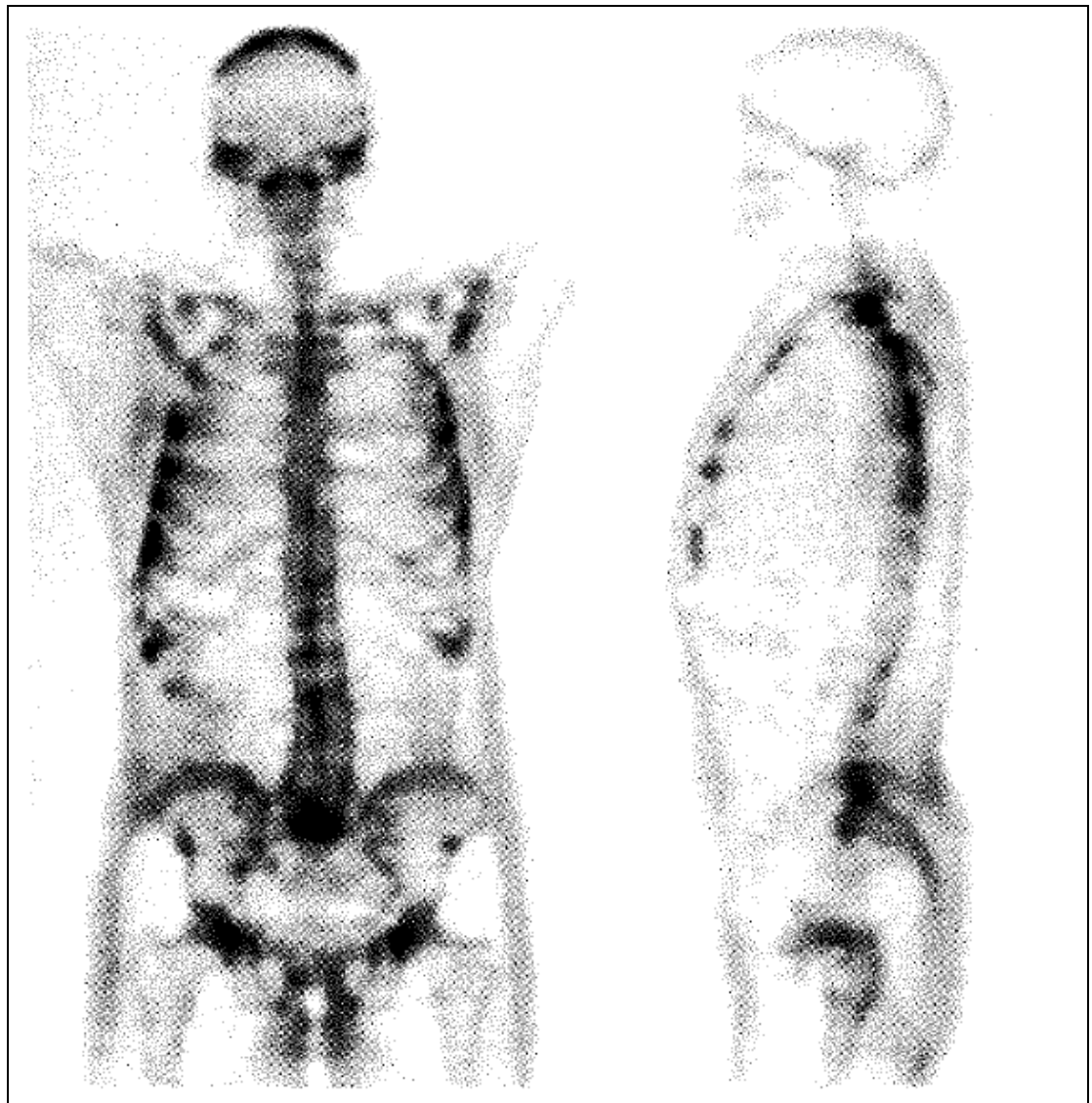


Figure 12: Zubal voxel phantom (skin, fat and bones highlighted)

3.2.3 BREP phantoms

Boundary representation (BREP) computational phantoms contain exterior and interior anatomical features of the human body developed using the NURBS method or polygon mesh method – collectively known as the boundary representation method. A solid is represented as a collection of connected surface elements using the BREP technique.

There are two types of information in the BREP: topological and geometric. Topological information provides the relationships between vertices, edges and faces, and includes information on the connectivity between geometric shapes. Figure 13 depicts a lung defined by the CSG modeling technique (a), voxel modeling technique (b) and BREP modeling technique (c) [19].

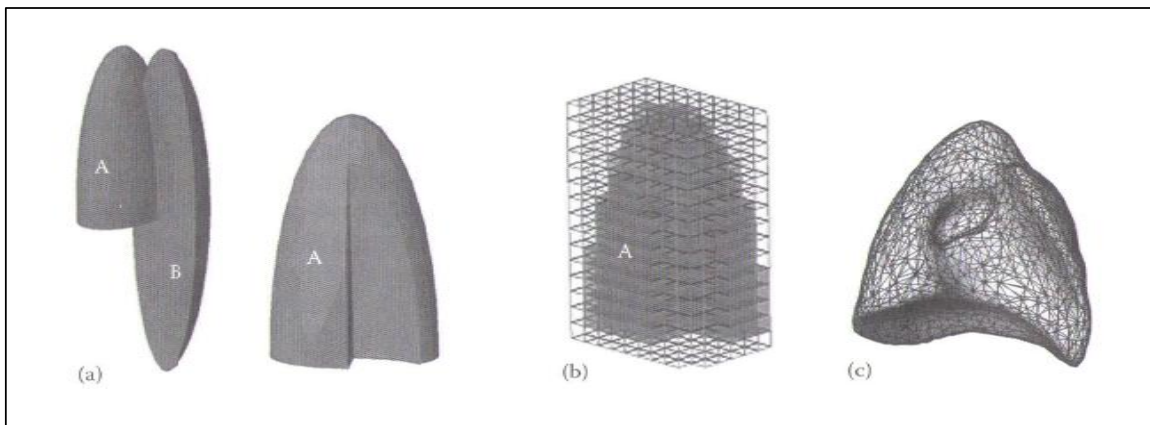


Figure 13: A lung defined by the (a) CSG, (b) voxel and (c) BREP modeling techniques

An extension of BREP is the non-uniform rational basis spline (NURBS) modeling technique. NURBS is a mathematical model for generating and representing curves and surface (see Figure 14 for an example [42]). The shape of the surface is determined using control points (green nodes). A user can

manipulate the control points to achieve the desired surface. In the context of phantom development, a user may trace surfaces of CT or MRI data sets using a NURBS program to create BREP phantoms.

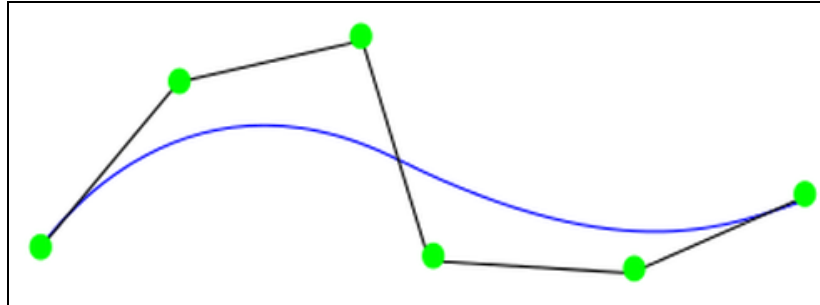


Figure 14: A curved line represented using the NURBS method

BREP computation phantoms are uniquely suited for surface deformation. The geometry may be deformed to fit particular organ shapes, volumes or body postures. Surface deformation allows for modeling the cardiac system and respiratory functions with a time-dependency – referred to as 4D modeling.

The earliest publication of the NURBS based modeling technique for a computational phantom is by Segars [19][43]. Segars developed the NURBS-based Cardiac Torso (NCAT) phantom. As the name implies, the phantoms only includes the torso; the legs arms and neck are not modeled (Figure 16).

The NCAT phantom was developed from the Visible Human CT image set [44] as the basis. The Visible Human image set is a complete digital image data set of complete human male and female cadavers in MRI, CT and anatomical modes. MR images of the head and neck were taken at 4 mm intervals; CT images of the entire body were taken at 1 mm intervals, resulting in over 5000 anatomical images. Figure 15 depicts an axial slice of the torso and arms of the male Visible Human image set.



Figure 15: One axial slice of the male Visible Human image set

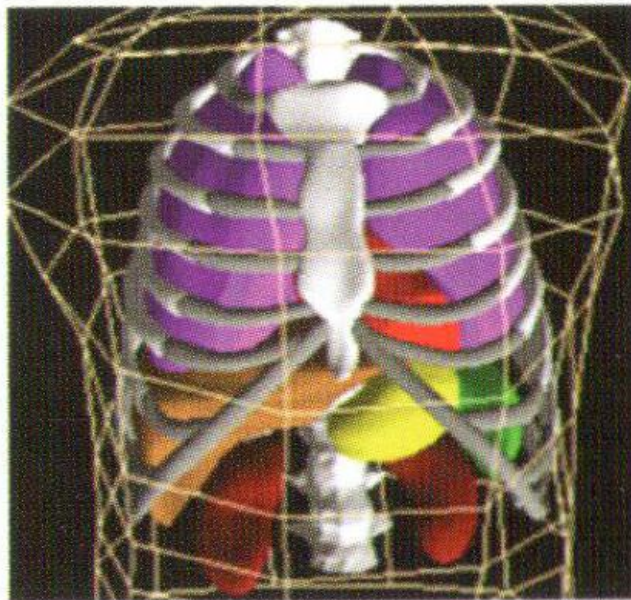


Figure 16: NCAT phantom

The NCAT was extended to model time-dependant cardiac and respiratory functions [45][46]. The cardiac motion was based upon 4D tagged MRI data sets obtained from the Johns Hopkins University. Respiratory motion was based upon a set of respiratory-gated CT data from the University of Iowa of a volunteer at 5%, 40%, 75% and 100% of his/her total lung capacity. The NURBS surfaces were fit to the image data to create a time-continuous model of the cardiac and respiratory functions. An animated GIF of the 4D NCAT anatomical motion is available on the computational human phantom Wikipedia page [47].

3.3 Selection of computational phantoms

Xu and Eckerman describe in detail a total of 28 BREP phantoms, 74 voxel phantoms and 8 stylized phantoms in their text [19] for a total of 110 unique computational phantoms. Many of the phantoms, particularly the voxel phantoms, are based upon a specific body type or a specific CT or MRI image set. The phantoms considered in this thesis should be based upon the same body size and anatomical data to facilitate a meaningful comparison of the phantoms for the Monte Carlo evaluation of the measurement efficiency of the PM12 for internal contamination. Further, comparing phantoms within the one of the three categories described by Xu and Eckerman (stylized, voxel and BREP) will not provide a meaningful assessment of the advantages of a specific modeling style.

In the phantom selection process the stylized phantoms represented the limiting factor. There are far fewer stylized phantoms than voxel and BREP phantoms (a total of 8 stylized phantoms); thus, there are far fewer stylized phantoms to cull. Also, the stylized phantom represents the greatest difference in anthropomorphicity between all three phantom categories, making it an ideal candidate for comparison with the more anthropomorphic voxel and BREP phantoms.

The MIRD stylized phantom developed at ORNL was selected for this study. The MIRD phantom, developed by Fisher and Snyder [17][21], is the earliest recorded anthropomorphic phantom. The original Fisher-Snyder phantom was defined by three shapes of tissue equivalent material. Snyder later improved the phantom, now called the MIRD-5 phantom, to be heterogenous [37][38], composed of three regions: skeleton, lungs and the remainder approximated as soft tissue. Most recently, the MIRD phantom was updated by Han under the direction of Bolch at the University of Florida (UF) in conjunction with Eckerman at ORNL [48]. The phantom was updated to include the tissue composition data from ICRP publication 89 on the revised reference anatomical data [49]. The updated phantom is now referred to as the UF-ORNL phantom.

ICRP publication 110 [50] includes a voxel data set based upon the reference anatomical data described in ICRP 89. The ICRP voxel phantom for the adult female and adult male are based upon CT image data sets from individuals with a height and weight similar to that of the reference data (ICRP 89). The data for the male voxel phantom was taken from a whole-body CT scan

of a 38-year-old male who suffered from leukaemia. The illness was such that it would not appear in the image data. The female voxel data was based upon a whole-body CT scan of a 43-year-old woman who also suffered from leukaemia. Adjustments were made to the male and female data sets to alter the size of the phantom and some organs so that it represented the reference data in ICRP 89.

The ICRP male voxel phantom was selected for this study as it based upon the same anatomical data as the UF-ORNL stylized phantom. It also represents a significant improvement in anthropomorphicity, allowing a study of the affects of anthropomorphicity on the Monte Carlo analysis.

The adult male BOMAB phantom was also selected for this work. The BOMAB phantom is the standard for calibrating WBCs [7]. The advantage of the BOMAB phantom is that it exists as both a computational and a physical phantom. Laboratory experiments may be performed to assess the accuracy of the Monte Carlo model by comparing empirical measurements with a physical BOMAB phantom with Monte Carlo calculations using a computational BOMAB phantom. This process is known as benchmarking. The BOMAB phantom is based upon the older reference data from ICRP 23, which is considered in the analysis.

A BREP phantom was not selected for this work. The advantage of the BREP phantom is the ability to perform simulations to assess the effect of cardiac and respiratory motion on a measurement system. The affect of cardiac and respiratory motion on the measurement efficiency of the PM12 for internal contamination is not considered in this thesis. The affect of respiratory motion on

counting efficiencies is normally of concern for lung counting systems where the measurement system is located very close to the chest wall [52]. Phantoms developed using the BREP technique do not represent an improvement in anthropomorphicity compared to voxel phantoms. For these reasons a BREP phantom was not considered for this thesis.

In conclusion, three phantoms were selected for this work: the UF-ORNL stylized phantom, the ICRP reference male voxel phantom and the adult male BOMAB phantom.

3.4 Monte Carlo radiation transport software

A Monte Carlo analysis code is required to perform radiation transport simulations with the computational phantoms selected for this study. In essence, radiation particles are originated inside of the computational phantoms. The path and interactions of the particles with the materials of the model are simulated using Monte Carlo techniques. Tallies are used to track the energy deposition of the particles in areas of interest such as a radiation detector. The response of the detector for the model geometry can be accurately calculated if a sufficient number of particles are simulated.

Several Monte Carlo codes exist that perform radiation transport simulations. Xu and Eckerman review some of these in their text [19]. These are summarized below.

The Monte Carlo N Particle (MCNP) code developed and maintained by Los Alamos National Laboratory (LANL) is a general-purpose Monte Carlo Code that performs neutron, photon, electron or coupled neutron/photon/electron transport [28][53]. MCNP extended (MCNPX) extends the capability of MCNP by supporting additional particle types, new cross-section libraries, and the ability to use physics models for energies where tabular data are not available. Most recently LANL released new version of MCNP – MCNP6 – which at the time of writing this thesis was still in beta testing.

The Electron Gamma Shower (EGS) code developed and maintained by the National Research Council (NRC) of Canada is a general-purpose package for the Monte Carlo simulations coupled transport of electrons and photons in an arbitrary geometry for particles with energies from a few keV up to several TeV [54].

The Geometry and Tracking (GEANT4) code is a toolkit for Monte Carlo simulations of electromagnetic, hadronic and optical processes [55]. The energy range covers 250 eV to TeV.

The PENELOPE code performs Monte Carlo simulation of coupled electron-photon transport in arbitrary materials and complex quadric geometries. The code covers an energy range of a few hundred eV to approximately 1 GeV. The cross section data in the very low energy regions allows the calculation of radiation interactions at the cellular level.

FLUKA is a general-purpose Monte Carlo code system for an extended range of 60 different particles: photons and electrons from 1 keV to thousands of TeV, neutrinos and muons of any energy, hadrons of energies up to 20 TeV and all of the corresponding antiparticles, neutrons and heavy ions [57].

MCNP was selected as the radiation transport code to perform Monte Carlo analysis with the computational phantoms. MCNP is a well validated code and is widely used in the nuclear engineering, health physics and medical physics communities. MCNP and MCNPX have been successfully used for WBC efficiency calibrations using voxel and BOMAB computational phantoms [8]-[11]. In addition, the author was already familiar with this code.

MCNP input geometries were readily available for the UF-ORNL and ICRP voxel phantoms. The UF-ORNL input geometry was taken from the PIMAL software [59]. PIMAL allows the user to adjust bend and rotation of the arms at the shoulder and elbow and the legs at the hip and knee. The software will output a MCNP input card for the phantom in that position. The stylized phantom was used with no bend in the arms or legs to remain consistent with the voxel phantom and because a standing measurement position is used for the PM12. Figure 17 depicts the MCNP phantom as viewed in three-dimensions in the Moritz Geometry Tool (Moritz) software [60].

Moritz is an interactive geometry editor and viewing tool for MCNP and MCNPX. MCNP is provided with a visual editing and viewing software, Visual Editor (Vised) [61][62]. However, Vised is not able to read voxel input cards whereas it is possible to read these using Moritz. Moritz and Vised are both used

throughout this work for viewing and validating MCNP input cards

Health Canada (HC) Human Monitoring Laboratory (HML) provided the MCNP input card for the ICRP reference male voxel phantom. Capello et al. [53] describes the refinement of the voxel phantom based upon the CT image data set provided in ICRP 110. Figure 17 depicts the MCNP phantom as viewed in two-dimensions using Moritz software.

The production of physical BOMAB phantoms is performed using high density plastic. The tolerances on the BOMAB specifications are $\pm 10\%$ on the shell wall thickness, $\pm 15\%$ on the total volume of the phantom, and $\pm 5\%$ on the diameter and height of each BOMAB section (bottle). This means that no two BOMAB phantoms will be created with equal dimensions.

A physical male BOMAB phantom was made available by OPG for benchmarking measurements. The phantom was developed by CANUS Plastics Inc. The dimensions of the OPG BOMAB phantom are provided in a report by the manufacturer [63]. A computational BOMAB model was developed using dimension of the BOMAB phantom quoted in this report. The phantom bottles are all elliptical with outside dimensions provided in Table 2. An image of the computational model of the BOMAB phantom as viewed in the Vised dynamic 3D display is provide in Figure 17. The model was checked for geometry errors in Vised.

Table 2: BOMAB phantom dimensions

Bottle	Minor axis (cm)	Major axis (cm)	Height (cm)
Right calf	11.6	12.2	40.00
Left calf	11.8	12.3	40.00
Right thigh	14.8	15.8	39.90
Left thigh	14.9	15.9	39.90
Gut	18.8	33.9	20.10
Chest	19.5	29.2	41.70
Neck	14.9	15	9.50
Head	14.7	19.1	19.70
Right arm	9.5	10	58.10
Left arm	9.7	10.4	58.30

*Bottle wall thickness is 0.5 cm

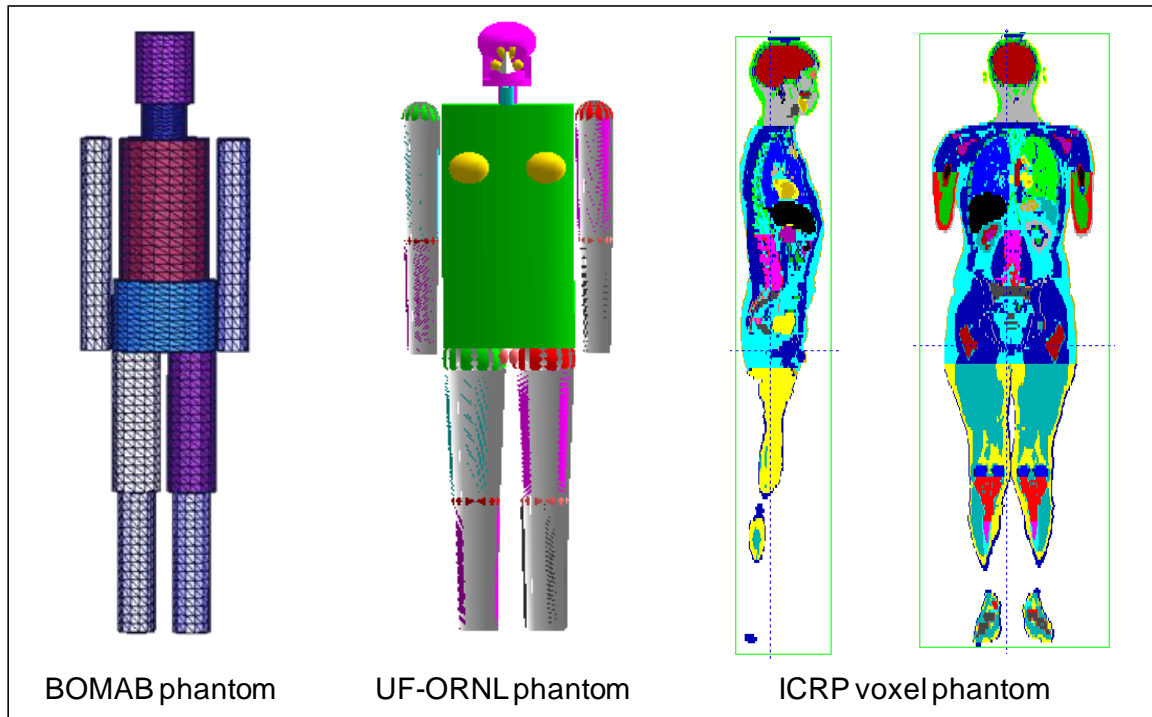


Figure 17: Phantoms considered in this study

3.5 Operational dose quantities

The Canadian Nuclear Safety Commission (CNSC) is the regulatory body for the control radioactive material in Canada to ensure the safety of the public, workers and the environment. The Radiation Protection Regulations (SOR) [6] published by the CNSC stipulates the expected requirements for dose management at facilities licensed to own and operate radioactive material or radiation devices (e.g., x-ray machine).

Dose limits for effective and committed doses are mandated in the SOR for three categories of persons:

- a) A Nuclear Energy Worker (NEW): someone who, as part of their occupation, is expected to receive a dose higher than the allowable dose limit for a member of the public;
- b) A pregnant NEW; and
- c) A member of the public: someone who is not a NEW.

The dose limits for these persons are provided in Table 3. The effective dose for external radiation exposures is calculated using Equation 4 [30]. The committed effective dose is calculated as the effective dose from intakes of radioactive material integrated over a period of 50 years for adults.

Table 3: Dose limits for NEWs and the public

Person	Period	Effective dose (mSv)
NEW	One-year dosimetry period	50
	Five-year dosimetry period	100
Pregnant NEW	Balance of the pregnancy	4
Member of the public	One calendar year	1

$$E = \sum_T w_T \sum_R w_R D_{T,R}$$

Equation 4

where

E is the effective dose (mSv);

w_T is the tissue weighting factor for tissue T;

w_R is the radiation weighting factor for radiation R;

$D_{T,R}$ is the mean energy imparted by ionizing radiation in a tissue T by radiation R (J/kg).

A common operational dose quantity for intakes of radioactive materials is the Annual Limit on Intake (ALI). The ALI is the intake (inhalation or ingestion) of a given radionuclide in a year by the reference man which would result in a committed effective dose equal to the relevant dose limit. The CNSC publishes ALI values for some radionuclides in its guidance document RD-52 [31] using dose conversion factors (i.e., Sv/Bq) for intakes from ICRP 68 [32]. The ALIs are calculated using Equation 5.

$$ALI = \frac{20mSv}{DCF}$$

Equation 5

where

ALI is the annual limit on intake (Bq) that corresponds to a committed effective dose of 20 mSv; and

DCF is the dose conversion factor for an inhalation or ingestion (Sv/Bq) from ICRP 68.

It is the responsibility of the licensee to ensure that effective and committed doses do not exceed the dose limits and to keep the doses as low as reasonably achievable (ALARA). Quoting from the SOR:

“Every licensee shall implement a radiation protection program and shall, as part of that program,

- a) Keep the amount of exposure to radon progeny and the effective dose and equivalent dose received by and committed to persons as low as is reasonably achievable, social and economic factors being taken into account...”*

The intent is that even though dose limits are provided by the CNSC, doses should be managed such that they remain low in respect of the work being performed. Action levels for exposures to radiation are built into the radiation protection program as dose control points for worker doses. If a worker dose reaches this control point it may indicate a loss of control of part of the licensee’s radiation protection program. An action limit for inhalation doses will be included in the radiation protection program at nuclear facilities where there is a risk of

aerosolizing radioactive material. The value of the action limit is selected based upon the operations at the facility. For the purposes of the research an intake of 1/10 ALI is considered operationally significant.

4. METHODOLOGY

4.1 Overview

The evaluation of the measurement efficiency of the PM12 as a function of time was performed for three computational phantoms. The process followed for the simulations is summarized in Figure 18.

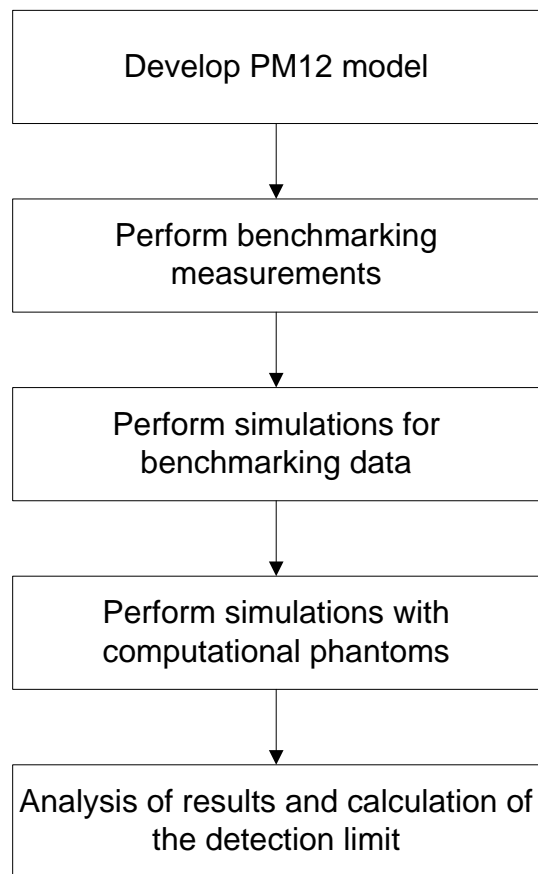


Figure 18: Methodology overview

4.2 Development of the PM12 model

The PM12 model was created to accurately represent the physical PM12 system based upon the information available on the system. Some features of the PM12 were not able to be modeled due to lack of information. Specifically these features include:

- a) The PMTs attached to the PVT detectors;
- b) The foil and aluminum jacket encasing each PVT detector; and
- c) Any electronics housed within the PM12

The physical specifications of the PM12 that were modeled were taken from the PM12 user manual, other brochures provided by the manufacturer [66]-[71], and a physical inspection of the device.

4.3 Performance of benchmarking measurements

Benchmarking measurements are necessary to validate the model of the PM12. The OPG campus in Whitby, ON provided access to their PM12 for benchmarking measurements. A total of four measurement studies were performed:

1. Characterization of the background readings for the PM12;
2. The response of each individual detector was measured using “button” radionuclide calibration standards (henceforth referred to as button sources) to ensure they were functioning as expected;
3. Measurements of the centroid efficiency with button sources; and
4. Measurements of the OPG PME series BOMAB phantom.

4.3.1 Background measurements

The detector count rate was measured in the absence of all sources to characterize the background noise in the detector. Source of background noise include: counts from naturally occurring radioactive material in the environment, counts from cosmic rays, counts from radiological contaminants in building materials, and counts due to electronic noise. This value of background counts (C_B) was subtracted from the measurement value (C_M) for the following experiments to calculate the net count rate (C_N)

$$C_N = C_M - C_B \quad \text{Equation 6}$$

4.3.2 Button source measurements

Measurements of each individual PVT detector of the PM12 were performed with a ^{241}Am , ^{137}Cs and ^{60}Co button source. These measurements were performed to confirm that each PVT detector was functional. These measurements are not used for benchmarking data.

The activities of the button sources, corrected to the date of the measurements, are provided in Table 4.

Table 4: Button source activities (adjusted to April 15, 2012)

Radioisotope	Half life (years)	Original activity (Bq)	Calibration date (MM/DD/YYYY)	Decay corrected activity (Bq)
^{60}Co	5.3	$3.96\text{E}+04 \pm 3.3\%$	04/15/1996	$4.88\text{E}+03$
^{137}Cs	30.1	$3.76\text{E}+04 \pm 3.3\%$	04/15/1996	$2.60\text{E}+04$
^{241}Am	432.2	$4.44\text{E}+04 \pm 3.3\%$	10/13/2005	$4.39\text{E}+04$

The center of each individual PVT detector located in the jamb is marked on the PM12 housing by a raised nub (Figure 19). The center of the ceiling and floor PVT detector was estimated to be equidistant from the edges and the front/back of the PM12. This distance was physically measured with a measuring tape. The button source was taped to the surface of the PM12 the individual PVT detector measurements.

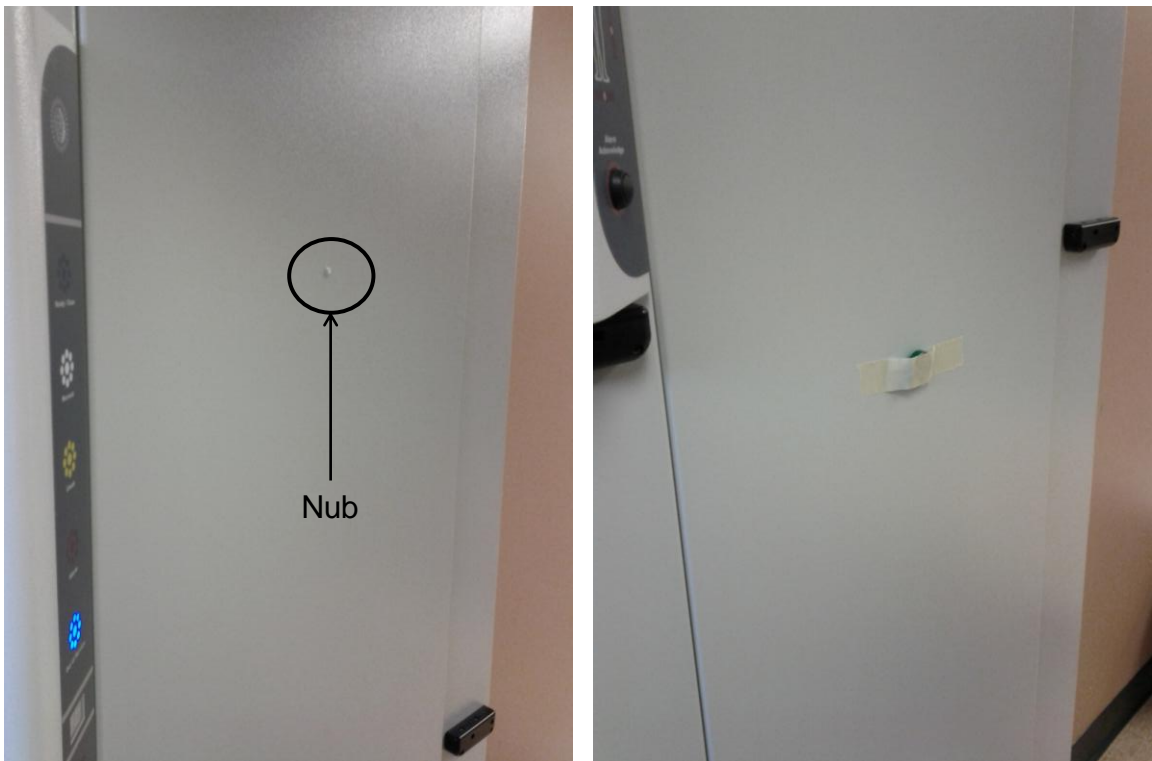


Figure 19: Positioning of the button source on a PVT detector

4.3.3 Centroid efficiency measurements

The centroid efficiency is the measurement efficiency for point sources in the geometric center of the PM12 (i.e., equidistant from all inside surfaces of the portal monitor). The centroid efficiency was measured for each of the button sources in Table 4.

The button source was positioned in the center of the PM12 using tape attached at both of the jambs. Geometric center of the PM12 was measured using a measuring tape. Figure 20 depicts the set up for the centroid efficiency measurements.



Figure 20: Centroid efficiency measurements

4.3.4 BOMAB phantom measurements

The OPG BOMAB phantom was erected and placed in the center of the PM12. A tape measure was used to position the BOMAB phantom. The BOMAB will not support itself without the use of a platform. A platform constructed of PVC pipe and a plastic surface was used to support the BOMAB phantoms (BOMAB support structure). Packing tape was used to add further support and to ensure the BOMAB phantom did not move if bumped during the measurements (Figure 21).



Figure 21: BOMAB phantom measurements

The effect of the plastic support structure on the measured signal was not measured. The attenuation from the structure can be approximated via a back-of-the-envelope calculation using the linear attenuation shielding formula (Equation 7)

$$I = I_o e^{-\mu \rho t} \quad \text{Equation 7}$$

where

I is the original photon beam intensity

I_o is the attenuated photon beam intensity

μ is the photon attenuation cross section of the absorbing material (cm^2/g)

ρ is the density of the absorbing material (g/cm^3); and

t is the thickness of the absorbing material (cm).

The photon attenuation cross section for the plastic support structure was taken from the XCOM online photon cross section database [72] for an elemental composition of CH, at an energy of 100 keV [$0.162 \text{ cm}^2/\text{g}$], the density of the plastic is assumed to be equal to that of water [$1 \text{ g}/\text{cm}^3$] and the thickness of the absorbing material was taken to be $\frac{1}{2}$ inch [1.27 cm]. Applying an arbitrary value for the original beam intensity of 1, the attenuated beam intensity is approximately 0.82; a reduction of 18%. Since the photon attenuation cross section decreases with increasing energy (Figure 22), the attenuation would decrease with increasing photon energy. Finally, the plastic support structure will mainly affect the photons emitted by the leg sections of the BOMAB phantom. Thus, the effect on the overall counting efficiency is expected to be low.

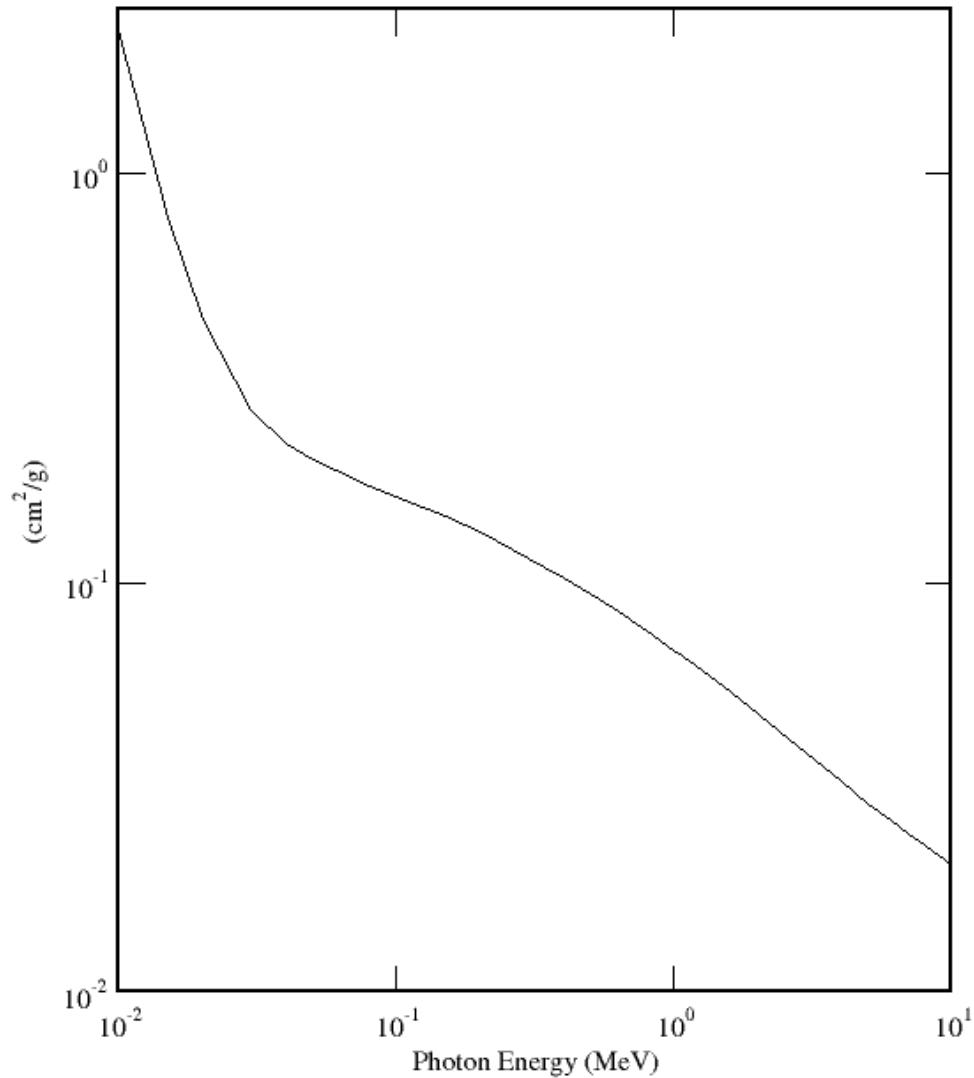


Figure 22: Photon attenuation cross section for CH from XCOM

The BOMAB phantom was filled with a liquid solution containing the radioisotopes and activities listed Table 5. No information was provided on the activity per bottle, thus it was assumed that the activity concentration (Bq/L) in each bottle is identical. The activity of the radioactive solution was confirmed by laboratory analysis by Kinectrics [64] (Annex A). The measured activity was used for the efficiency calculations. The activities are decay corrected to the date of the experiment.

Table 5: Activities of the BOMAB fill solution

Radioisotope	Expected activity (Bq)	Measured activity (Bq)
⁴⁰ K	6000 ± 300	5985
⁵⁷ Co	5010 ± 300	4910
⁶⁰ Co	3510 ± 180	3585
¹³⁷ Cs	4500 ± 200	4590

4.4 Performance of simulations for benchmarking data

Simulations were performed using MCNP version 5 to compare with benchmarking data from the physical measurements with the PM12. The simulations included the centroid efficiency and BOMAB phantom measurements.

4.4.1 Centroid efficiency

A point source was defined in the geometric center of the PM12 model. Four simulations were run in total which correspond to the radioisotopes in Table 4 and one additional isotope (⁵⁷Co) as its centroid efficiency is provided by the manufacturer. The gamma ray emission energies and yields (Annex B) – corrected for the branching ratio – for the source definition card were taken from the National Nuclear Data Center website [65]. Gamma and x-ray emissions below 20 keV and/or with yields less than 0.1% were not considered. The 20 keV energy cutoff is consistent with the PM12 energy cutoff stated in the user manual [63].

The simulations were run for one hundred million (10^8) particles. When simulating some of the gamma emissions with low decay probabilities (e.g., 692 keV gamma ray emitted from ^{57}Co with 0.16% decay probability), a large number of particles are required to properly sample that gamma ray to reduce relative errors and increase the confidence interval of the tally.

4.4.2 BOMAB simulation

The BOMAB computational phantom was coded into the MCNP input card for the PM12 computational model. The BOMAB computational phantom was positioned in the center of the PM12 model, equidistant from the front and back and the sides (Figure 23). This represents the measurement geometry applied in the benchmarking measurements. The geometry was visually checked for errors using VisEd software.

The photon emission rates and yields from Annex B were included in the source definition (sdef) card. Each bottle was included in the source distribution. The particle frequency for each bottle was weighted by the bottle volume to ensure a uniform distribution of source particles across the whole phantom.

The simulation was run for twenty million (2×10^7) particles.

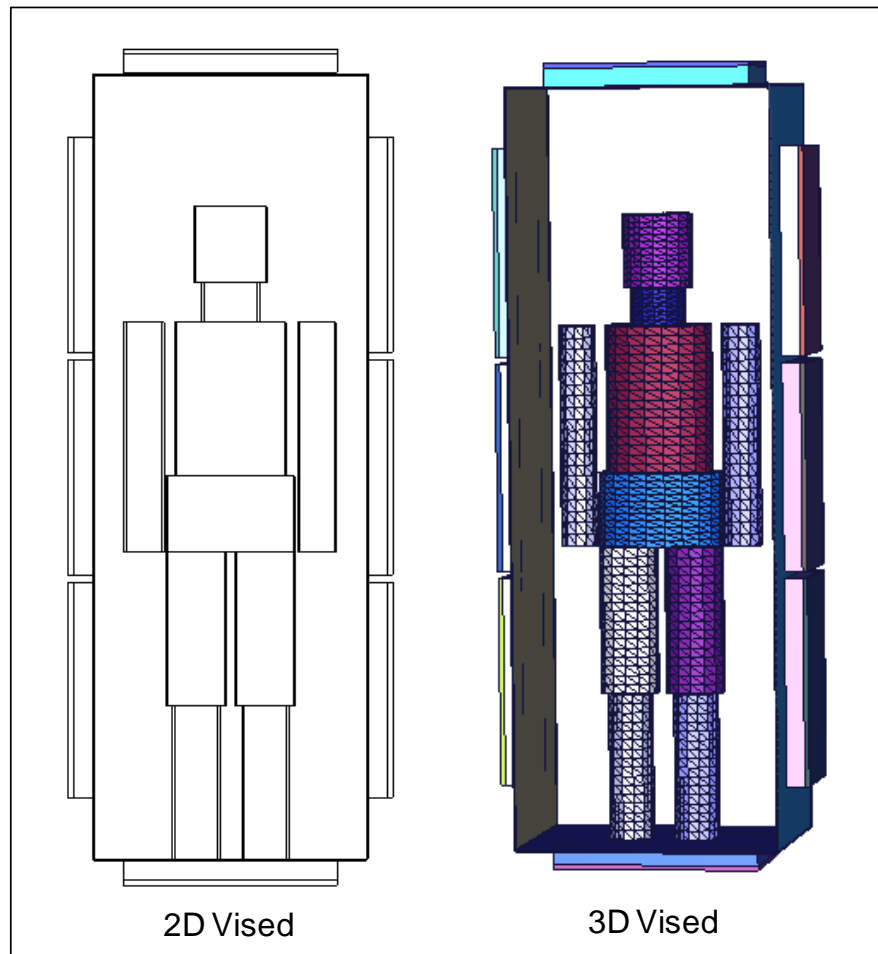


Figure 23: BOMAB computational phantom inside of the PM12 model

4.5 Development of counting efficiency curves

MCNP simulations were performed for the BOMAB phantom and UF-ORNL stylized phantom in MCNP5. The ICRP reference male voxel phantom will not run in MCNP5. MCNP5 is not able to open the large voxel lattice (over 31,000 lines of code). This observation is confirmed by Kramer [11]. The voxel phantom simulations were run successfully in MCNPX.

The source distribution was modeled to be in the phantom lungs. The BOMAB phantom has no lungs, thus the source distribution was modeled in the chest bottle. This is reflective of an inhalation scenario. Other contaminating scenarios (e.g., ingestion) were not modeled.

MCNP VisEd was used to confirm the source distribution using the plot source function (Figure 24). The ICRP voxel phantom contains too many lines of code to be opened in MCNP VisEd. Moritz was used to confirm the source distribution for the ICRP voxel phantom by opening an output file run for 1000 particles and plotting the particle tracks to ensure the particle flux is at a maximum in the lungs.

Simulations were performed for monoenergetic photons with the following energies in keV: 60, 112, 279, 662, 1173, 1332, and 2000. These energies roughly correspond to the main gamma emissions of ^{241}Am , ^{57}Co , ^{203}Hg , ^{137}Cs and ^{60}Co respectively with 1173 and 1332 keV both being emitted by ^{60}Co . 2000 keV does not correspond to the quoted radioisotopes, but was added to extend the energy range of the efficiency calculation. The extended energy range is useful to develop counting efficiencies for radioisotopes with gamma-ray emissions between 1332 and 2000 keV, such as ^{40}K (1400 keV).

Simulations were run for 20 million (2×10^7) particles.

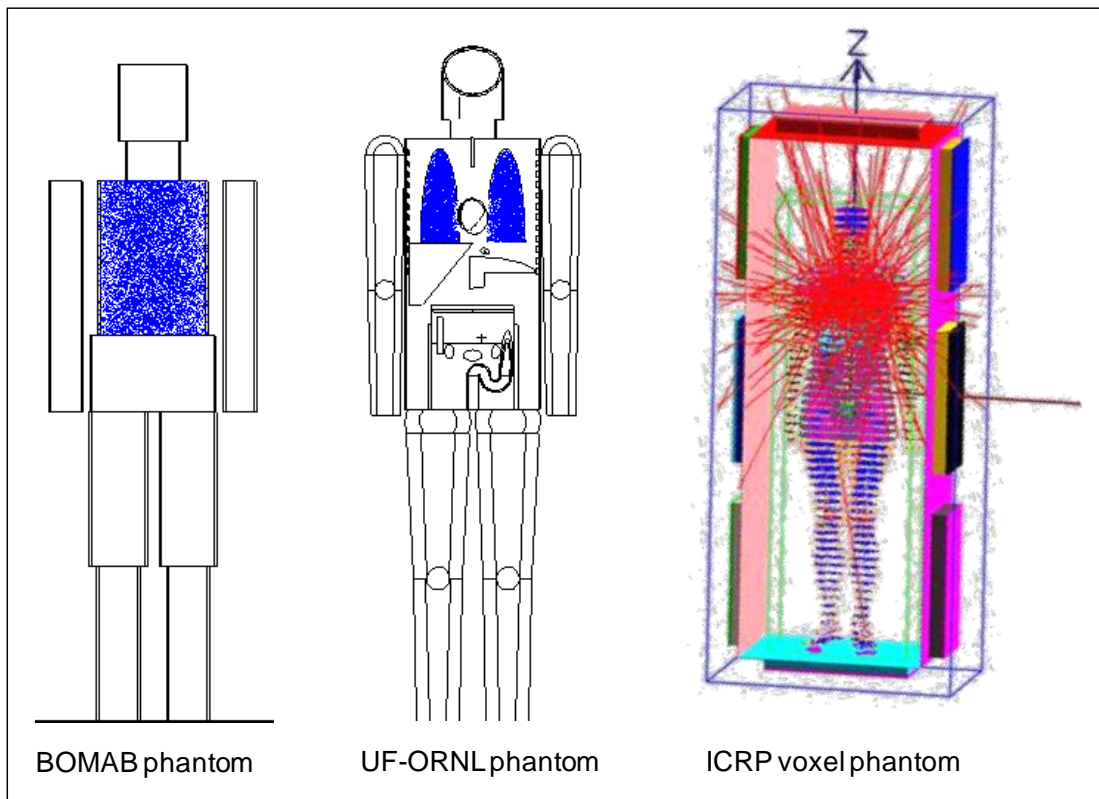


Figure 24: Plotting the source distribution for each computational phantom

4.6 Calculation of the detection limit

Knoll [25] defines the detection limit as the smallest signal that can be detected reliably. In the simplest counting system, two measurements are performed: a measurement of an unknown sample (C_M) and a measurement of a blank sample to determine the background level (C_B). The net counts (C_N) are calculated using Equation 6.

The detection limit is solved in two parts. First there must be a criterion for deciding that the sample doesn't belong to the background distribution, i.e., at what measured level above background can we decide that the sample contains net activity –the decision level (L_D). The decision level is solely based on the

dispersion of the background measurements. Second, there is a criterion for deciding when the net activity is sufficiently large – the detection limit (N_D). The detection limit takes into account the dispersion of the measurements for the background and the sample.

Figure 25 depicts the concept of the decision level and the detection limit. Where α is the probability of a false positive, β is the probability of a false negative and k_α and k_β is the coverage factor (in units of standard deviations) that corresponds to the probability of false positive (α) or false negative (β).

A false positive is when the system indicates that there is activity (Bq) in the sample when, in fact, no contamination is present and only background radiation has been measured. A false negative is when the system indicates that there is no activity in the sample when, in fact, activity is present in the sample.

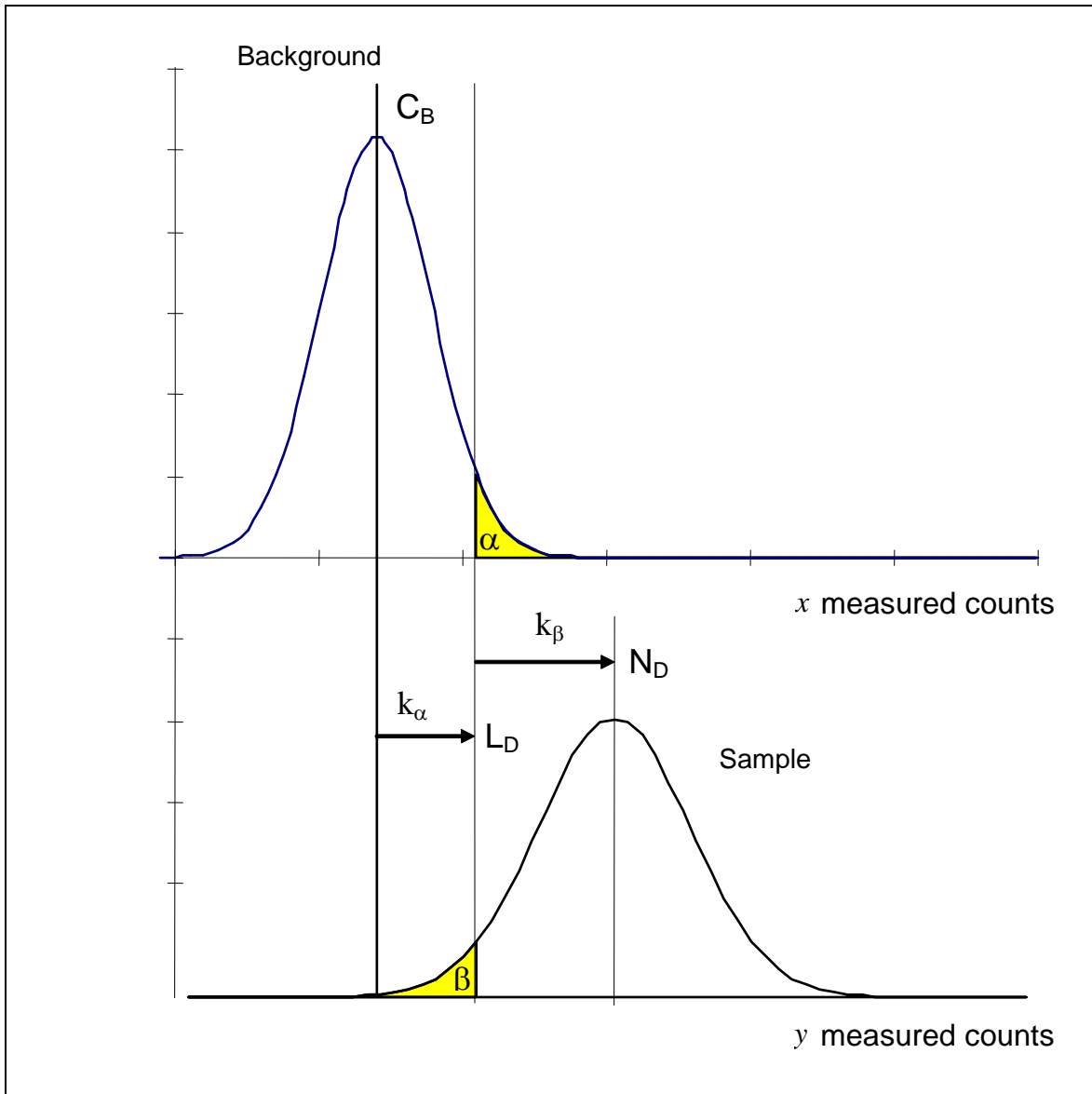


Figure 25: Depiction of the decision level and detection limit

The PM12 user manual [68] provides the equation used by the on-board software to calculate the detection limit in terms of a count rate (R_D), given by Equation 2. Note that N_D is the detection limit for a sample count and R_D is the time integrated detection limit expressed as a count rate. Equation 2 simplifies to a second degree polynomial for R_D and may be solved using the quadratic equation.

$$R_D = k_\beta \sqrt{\frac{B_{eff}}{t} + \frac{B_{eff}}{s}} + k_\alpha \sqrt{\frac{B_{eff}}{t} + \frac{B_{eff} + R_D}{s}} + \frac{1}{4} (k_\beta + k_\alpha)^2 \left(\frac{1}{t} + \frac{1}{s} \right) \quad \text{Equation 8}$$

where

t is the count time of the background (seconds);

s is the count time of the sample (seconds);

B_{eff} is the sum of the mean background count rates for all of the detectors (cps); and

R_D is the detection limit expressed as a count rate referred to as the minimum detectable count rate (cps).

The minimum detectable activity (MDA) was then calculated from the PM12 detection limit using Equation 3. The product of f and ϵ is summed for each gamma ray emitted from the radioisotope.

$$MDA = \frac{R_D}{\sum_i f_i \times \epsilon_i} \quad \text{Equation 9}$$

Where

f_i is the gamma yield per disintegration for gamma ray emission i ; and

ϵ_i is the detection efficiency for gamma ray emission i .

The gamma yield is radioisotope specific. The gamma yield values are provided in Annex B. The detection efficiency is taken from the MCNP PM12 efficiency calculations.

As discussed in Section 3.5, the ALI is the quantity of a radioisotope that will lead to a committed effective dose of 20 mSv when inhaled or ingested. The MDA (Bq) can be converted into a number of ALIs (Bq) by taking the ratio of the MDA to the ALI. The sample time require to achieve an MDA corresponding to 1/10 ALI will thus be calculated.

5. RESULTS AND DISCUSSION

5.1 Development of the PM12 model

5.1.1 Description and specifications of the PM12

The physical dimensions of the PM12 are provided in Section 3.1 of this thesis. The physical dimensions were used as the basis for the development of the model. To supplement the modeling efforts a PM12 was physically inspected.

The Ontario Power Generation (OPG) Whitby campus owns a PM12 that was made available for physical inspection. The panels that cover the PVT detectors located in the jamb were removed. Figure 26 shows the positioning of the three detectors within the jamb. The detectors are located approximately 1 cm apart from each other.

The PVT detector is covered with a very thin foil casing. The foil provides a light tight environment so that the signal measured by the PMT is not affected by light not caused by scintillation in the PVT detector. This casing was not modeled as it was not possible to measure the thickness of the casing and, from visual inspection, the casing seemed sufficiently thin that it would cause minimal attenuation of photons.

The PM12 housing could not be further removed to inspect the internal electronics and other internal structures. Thus, these features could not be modeled. A 1" thick lead shield is located at the back of each PVT detector. This should be sufficient to effectively shield most photons that would scatter off of internal structures within the PM12 towards the PVT detectors.



Figure 26: PM12 with housing removed

5.1.2 Development of the PM12 model

The PM12 was modeled in MCNP based upon the specifications in the previous section. Only the inner housing, PVT scintillators and lead shielding were modeled. The area inside of the PM12 not occupied by the PVT scintillators and the lead shielding was assumed to be air.

The manual did not provide information on the location of the PVT scintillators within the housing. It was assumed that the floor and ceiling scintillators are located equidistant from both jambs. It was assumed that the middle jamb scintillator was located equidistant from the ceiling and floor and a 16 cm separation between the middle scintillator and the bottom and top jamb scintillators.

The MCNP Visual Editor (Vised) version 22S [61] was used to image the model and check for geometry errors. Figure 27 provides a screen capture of the model as viewed using the dynamic 3D display function of Vised.

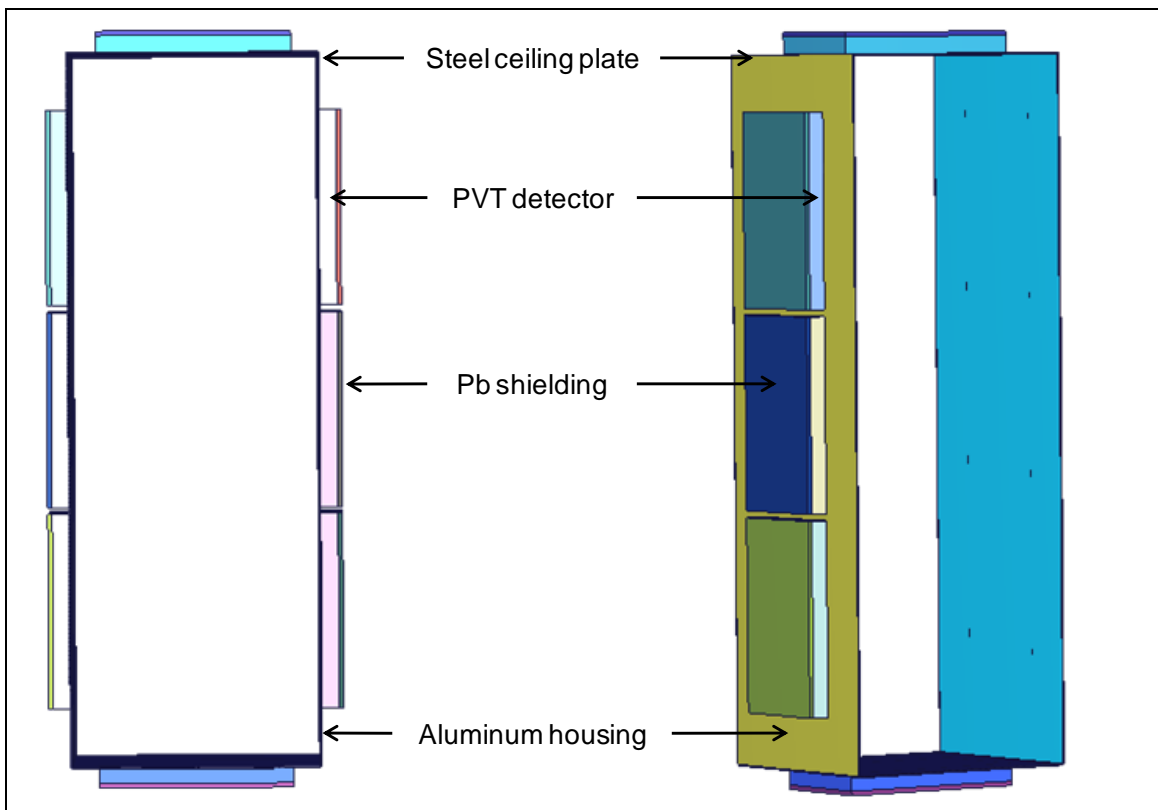


Figure 27: Model of the PM12

Table 6 provides the density and elemental composition for the PM12 materials applied in the MCNP model.

Table 6: PM12 material composition

Material	Density (g/cm ³)	Elemental composition		Reference
		Element	Mass/atomic* ratio	
Polyvinyl toluene (PVT)	1.032	H C	1* 1.104*	[72]
Lead	11.34	Pb	1*	
Stainless steel	7.8	Fe Cr	0.73 0.27	[74]
Aluminum	2.7	Al	1*	
Air	0.00129	N O Ar	0.78 0.21 0.1	[75]

5.1.3 Photon energy binning

The PM12 uses a similar radiation counting set-up to that shown in Figure 4. A PMT tube is attached to the PVT scintillator. The signal from the PMT is sent to a pre-amp to convert the low-amplitude, short duration pulse from the PMT into a voltage pulse, the amplifier shapes the pulse to meet the input requirements of the MCA and the MCA bins the electrical pulses based upon their amplitude.

The PM12 uses five energy bins with factory set energy thresholds.

Quoting from the Thermo 'frequently asked questions' brochure [71]:

Five energy thresholds are factory set in the PM12:

T1 is the lowest, set just above the noise level.

T2 is set at the 137Cs peak energy 662keV

T3 is set for higher energy levels (>700keV).

T4 is set just above the 60Co peak energy 1.3MeV

T5 is set at Cosmic energy level.

The pulse height tally (F8) in MCNP allows energy binning such as above. Some interpretation was required for the T1 and T5 thresholds as their energy is not provided.

This study is interested only in energy response from anthropogenic sources. The 0.05 - 2 MeV energy range brackets many of the radionuclides that may be found in an occupational setting (e.g., ¹³⁷Cs and ⁶⁰Co). This will be the energy range over which the response of the PM12 is studied.

As the maximum energy of this study is 2 MeV, the T5 threshold is not important, as long as it is set above 2 MeV. Therefore an energy of 10 MeV was selected for the T5 threshold. The T1 threshold was difficult to predict as it is set “just above the noise level”. MCNP simulations are void of the background noise that real detector systems are subject to. In this sense the value of the T1 threshold is not important; however, MCNP is subject to “nonanalog” processes in the pulse height tally. Knock-on electrons, electrons knocked out of their orbital by fast energetic charged particles, in MCNP are nonanalog in that the energy loss is included in the multiple scattering energy loss rate rather than subtracted out at each knock-on event. Thus, knock-ons can cause negative energy pulse height scores. The MCNP5 manual [28]-[53] recommends an ‘epsilon bin’ from 0-10 eV to capture (and exclude) these nonanalog events. Thus, the T1 threshold is set to 10 eV.

The energy bins used for MCNP simulations for the PM12 response are provided below in MeV:

- 0 to 1E-5 (epsilon bin)
- 1E-5 to 0.662
- 0.662 to 0.700
- 0.700 to 1.4
- 1.4 to 10

5.2 Benchmarking measurements and simulations

5.2.1 Centroid efficiency benchmarking

Benchmarking measurements were performed with button sources and the BOMAB phantom at the OPG campus in Whitby, ON. The measurement geometry of the benchmarking measurements were replicated in MCNP and simulations were performed. The measurement data for the benchmarking measurements is provided in Annex C. Simulation results are provided in Annex D

The centroid efficiency was measured with three button sources (Table 4). The total counts in each energy bin were summed to yield the total count rate of the system. The background count rate was then subtracted from the total count rate to yield the net count rate. The measured value in counts per second was normalized by the activity of the source to produce the efficiency in counts per decay but presented as a percentage. The simulated values provided by MCNP are normalized to one photon (count/photon). The simulated value is multiplied by the total photon yield per decay to yield units of counts per decay; however this is also presented as a percentage. Thermo also provides centroid efficiency specifications for the PM12 as a percentage [66] measured according to the

International Electrotechnical Commission international standard IEC 61098 [67].

A matrix of the measured, simulated and quoted manufacturer specifications for centroid efficiencies is provided in Table 7. The results are also plotted in Figure 28.

Table 7: Centroid efficiency benchmarking results

Radioisotope	Simulated efficiency (%)	Measured efficiency (%)	Manufacturer's efficiency (%)
¹³⁷ Cs	8.17 ± 0.003	8.51 ± 0.045	8.60
⁶⁰ Co	15.37 ± 0.1	14.51 ± 0.11	17.10
²⁴¹ Am	0.28 ± 0.001	0.39 ± 0.024	N/A
⁵⁷ Co	8.63 ± 0.1	N/A	4.60

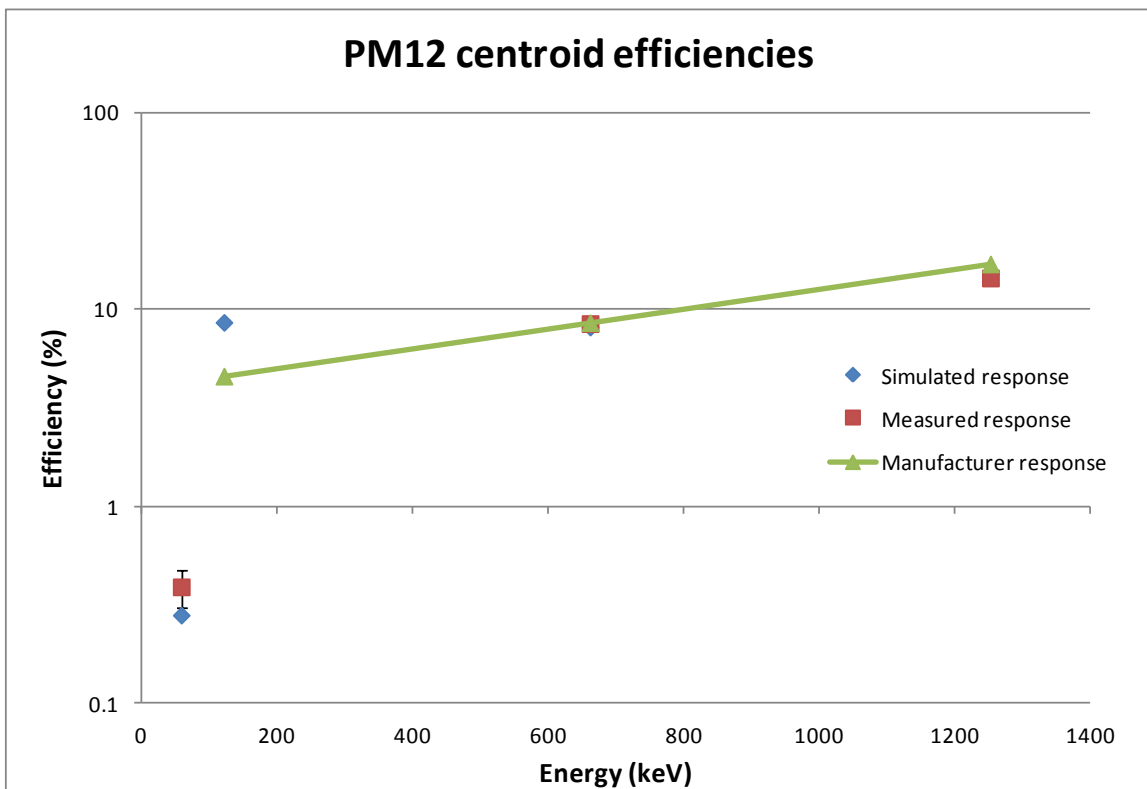


Figure 28: PM12 centroid efficiencies (simulated, measured and manufacturer)

The values for the simulated, measured and manufacturer's centroid efficiency fit well for ^{137}Cs and ^{60}Co with the maximum percent difference of the values being 5% (between the simulated and manufacturer's) and 16% (between the measured and manufacturer's) respectively. The percent error between the simulated values and the measured or manufacturer's values for ^{241}Am and ^{57}Co are higher at 33% and 61% respectively.

A line is plotted through the manufacturer response data in Figure 28 to show that the quoted response is log-normal. The measured data does not support this.

In general, the simulations agree with the measurements for energies exceeding 662 keV. The model under-responds by 33% at 59 keV. From a radiation safety point of view this is acceptable as the model will estimate the activity of internal contamination to be higher than the true value, thus remaining conservative.

Either measurement error or simulation error could lead to the discrepancies between the measured and simulated value. These errors are discussed in Table 8.

Table 8: Sources of error between measure and simulated centroid efficiencies

Error	Error description	Discussion
Measurement errors		
Source placement	The placement of the button source in the PM12 was not exactly centered. Since the detector is symmetrical, incorrect positioning of the source would lead to an increase in one detector and a decrease in the other which may be approximated by the inverse square law.	If the source was positioned incorrectly (i.e., closer to one side of the PM12) the response in the detectors closest to the source would increase and the reverse would be true for the detector furthest from the source. Due to the symmetry of the PM12 the ratio of the detector response on one side to its mirrored counterpart should be unity. The ratio of each detector was taken to its mirror counterpart. The ratios were within a couple percent of unity for all measurements.
Measurement error	The statistical error on the measured value.	The relative errors of the measured efficiencies for ^{137}Cs and ^{60}Co are less than 1%. The relative error on the ^{241}Am measured efficiency is 6.2%
Source activity error	Errors on the activity calibration of the button sources could lead to errors in the measured efficiency.	The error on the activity calibration of the button sources specified by the manufacturer is 3.3%. The button source activities were decay corrected of the date of the experiment.
Simulation errors		
MCNP simulation error	The statistical error of the simulated values	The relative errors on the MCNP simulations were approximately 1%. According to Table 1, these results are reliable.

Error	Error description	Discussion
Limitations of the computation model	Section 5.1.1 identifies a number of features of the PM12 that could not be modeled due to lack of information.	Differences between the physical model and computational model could lead to significant difference between simulations and measured results. Also, variations in the thickness of the absorbing material have a more pronounced effect for lower energy photons.

The main contributing factor to the variations between measured and simulated counting efficiencies is likely the limitations of the PM12 computational model. Figure 29 depicts the photon absorption coefficients for some common metals with lines at the approximate location of the gamma-ray emission energies for ^{241}Am , ^{137}Cs and ^{60}Co . there is an order of magnitude difference between the photon absorption coefficients for ^{241}Am and ^{60}Co in aluminium (the material of the PM12 housing). Applying Equation 7, increasing the thickness of the aluminum shielding from 1/8" to 1/4" would increase the attenuation of the ^{241}Am gamma-rays relative to the ^{60}Co gamma-rays by 50%.

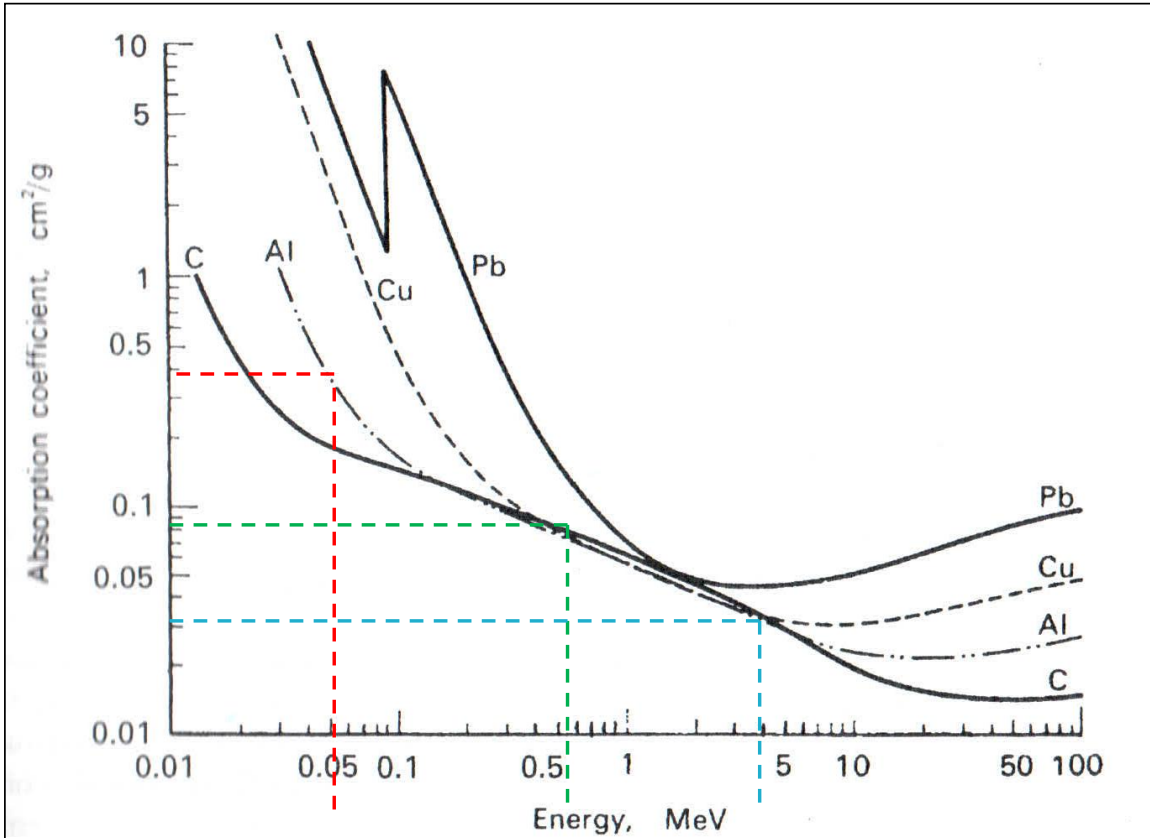


Figure 29: Photon absorption coefficients for some common elements [25]

5.2.2 BOMAB phantom benchmarking

Benchmarking measurements were performed of the BOMAB phantom at the OPG campus in Whitby, ON. The experimental setup is shown in Figure 21. The measurements in units of counts per second were normalized by the total activity of all the isotopes in the phantoms to yield units of counts per decay. The efficiency is presented a percentage.

The experimental setup was replicated in MCNP with the BOMAB computational phantom and separate simulations were run for the ^{60}Co , ^{57}Co , ^{137}Cs and ^{40}K gamma ray emission energies and yields. The simulated values provided by MCNP are normalized to one photon (count/photon). The simulated

value is multiplied by the total photon yield per decay to yield units of counts per decay; however this is also presented as a percentage.

The results of the BOMAB phantom measurements and simulations are provided in Table 9.

Table 9: BOMAB phantom benchmarking results

Radioisotopes	Measured efficiency (%)	Simulated efficiency (%)
⁵⁷ Co	5.98	5.64
⁶⁰ Co		
¹³⁷ Cs		
⁴⁰ K		

The measured and simulated measurement efficiency agrees well with a percent difference of approximately 5.7%. The centroid efficiency measurements showed that the model under responds at low energies (< 122 keV). It is possible that the model responded accurately for the BOMAB simulations as the majority of the activity was from radioisotopes that emit high energy (> 662 keV) gamma rays. Looking at gamma ray yield alone, ⁵⁷Co contributes less than 1% to the total photon emission rate from the BOMAB. The majority of the gamma ray emission rate (over 50%) comes from ⁶⁰Co.

5.2.3 Counting efficiency curve simulations

Simulations were performed for the BOMAB, UF-ORNL and ICRP reference male voxel phantoms to calculate the efficiency as a function of energy. The efficiencies provided here are the sum of the efficiencies of the eight PVT detectors. The simulation parameters are described in the methodology section (Section 4.5). To reiterate, the source distribution was modeled in the

lungs of the UF-ORNL and ICRP voxel phantoms and in the chest section of the BOMAB phantom. The BOMAB and UF-ORNL phantom simulations were run in MCNP 5 whereas the voxel phantom was run in MCNPX. The UF-ORNL phantoms simulations were also run in MCNPX to investigate any difference in results between the two codes. The result provided by MCNPX was identical to that provided by MCNP5. MCNP5 was used for the BOMAB and UF-ORNL counting efficiency simulations as these simulations were run first and the issue with the voxel phantom not running in MCNP5 was unknown at that point in the research.

The calculated efficiency curves are depicted in Figure 30 and a bias plot of the percent difference between the BOMAB is provided in Figure 31. The bias plot uses the BOMAB efficiency as a baseline (i.e., equal to 1) and shows the percent different between the BOMAB counting efficiency and the UF-ORNL and ICRP voxel phantom efficiencies as a function of energy.

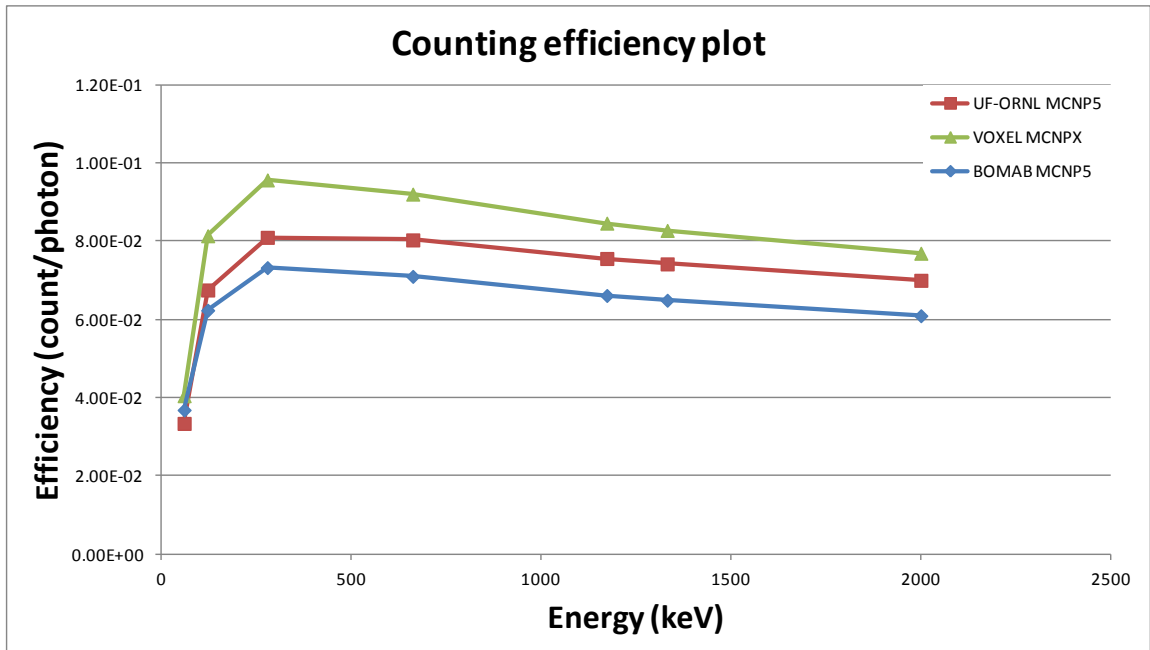


Figure 30: Efficiency curves for three computational phantoms

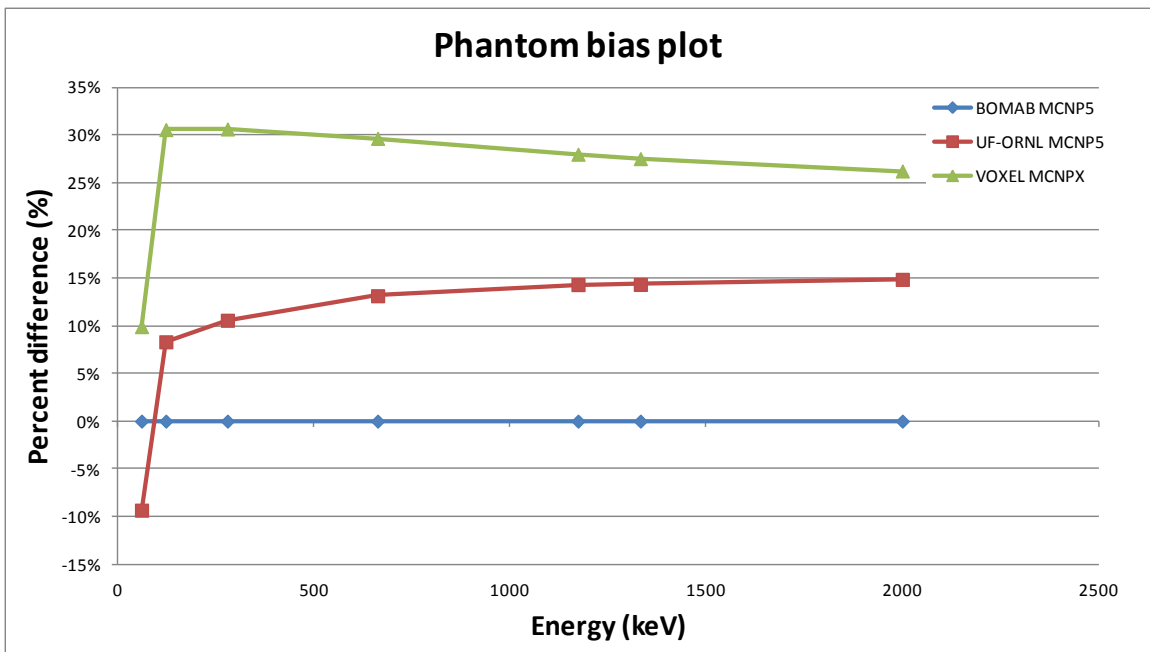


Figure 31: Bias plots for three computational phantoms

The measurement efficiencies are highest for the voxel phantom and lowest for the BOMAB phantom with a 26% percent difference at 662 keV. The higher counting efficiency for the voxel phantom compared to the BOMAB phantom is consistent with the findings of Capello [53]. The bias (ratio) between the voxel phantom and the BOMAB phantom is much less, approximately a few percent, as calculated by Capello. The source distribution included the following organs for Capello's work: muscles, thalamus, thyroid, gall bladder, liver, kidneys, pancreas, spleen, thymus, bladder, heart, adrenal gland, and reproductive system, resulting in 43% of the phantom being radioactive. This work only considers a source distribution in the lungs. The source being more localized in the simulations performed for this work could explain this discrepancy.

The bias plot shows a steep drop off at low energies (< 100 keV) for the UF-ORNL and ICRP voxel phantoms. One contributing factor is that the lungs are more accurately modeled in the UF-ORNL and ICRP voxel phantoms. Particles originating at the edges of the BOMAB phantom are more likely to escape to be measured by the PM12, whereas the particles originating in the lungs of the stylized and voxel phantoms must travel through several cm of tissue to escape the body. The source distribution plots in Figure 24 depict this phenomenon. At higher energies (> 100 keV) the bias is relatively consistent; within approximately 5%.

5.3 Calculation of the detection limit

The detection limit in terms of a count rate (R_D) was calculated as a function of sample count time using Equation 8. The default settings for the parameters of the probability of a false negative (k_α), the probability of a false positive (k_β), and the time over which the background counts have been average (t) are given in the user's manual. The sum of the mean background counts (B_{Eff}) for all of the detectors was taken from the benchmarking measurement data (Annex C). These constants are provided in Table 10.

Table 10: Constants for detection limit measurements

Parameter	Variable	Default setting	Units
probability of a false negative	k_α	1	Standard deviations
probability of a false positive	k_β	3.1	Standard deviations
Background count time	t	100	Seconds
Sum of the mean background counts	B_{Eff}	5552	cps

The sample count time (s) is not given in the user's manual. The goal is to keep count times short to increase throughput. The detection limit was assessed for a range of values of s using Equation 8. The detection limit is presented as a net count above background in Table 11 and plotted as a function of sample time in Figure 32.

Table 11: Detection limit as a function of sample time

Value of s (seconds)	PM12 detection limits (cps)
1	244
2	174
5	111
10	81
15	67
20	59
50	42

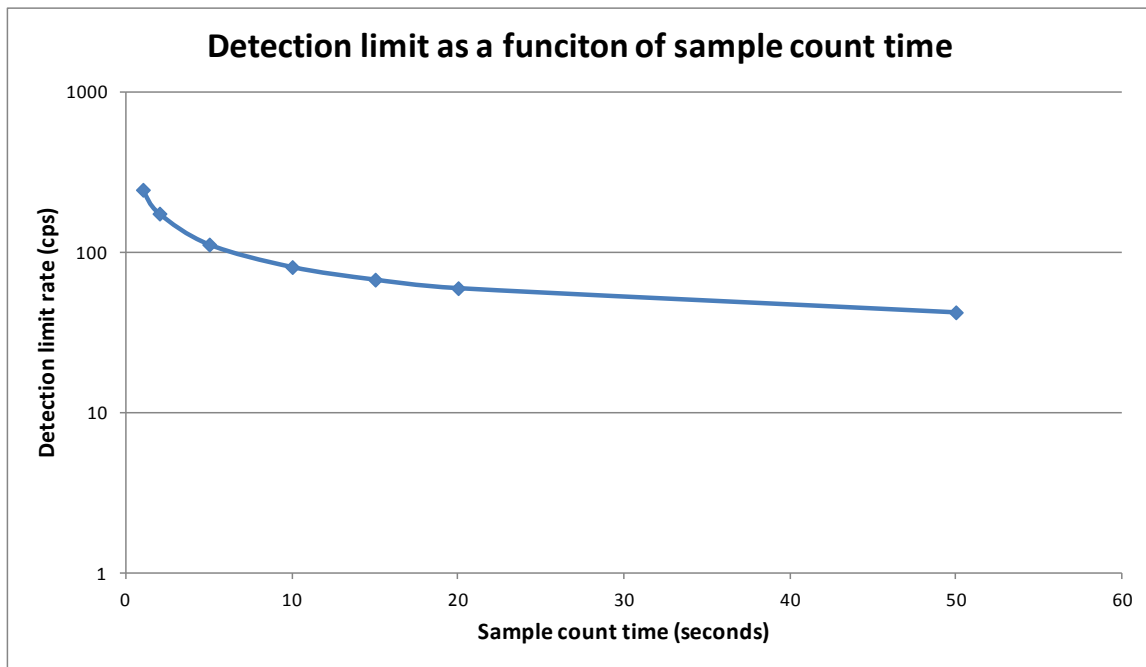


Figure 32: Detection limit as a function of sample count time

The minimum detectable activities (Equation 9) for ^{241}Am , ^{57}Co , ^{60}Co , ^{137}Cs and ^{40}K were calculated as a function of sample time using Equation 9. The calculated counting efficiencies (ϵ_i) for the BOMAB computational phantom were taken from Figure 30, the photon yields (f_i) were taken from Annex B and the calculated PM12 detection limits (R_D) were taken from Figure 32. The calculated

MDAs are provided as a function of sample time in Table 12 and plotted in Figure 33. Gamma ray emission energies that were not directly simulated (e.g., 1460 keV for ^{40}K) were linearly extrapolated or interpolated.

The uncertainty on the MDA is estimated from the standard deviation on the net count rate and the uncertainty on the measurement of activity due to chest wall thickness. The most conservative value of the uncertainty on the measurement due to chest wall thickness reported by Kramer [76] of a factor of 1.2 is used for the uncertainty assessment. The uncertainties are summed in quadrature to estimate the uncertainty on the MDA (Table 12).

Table 12: MDAs calculated as a function of sample time

Value of s (seconds)	Uncertainty (%)	MDA (kBq)			
		^{241}Am	^{57}Co	^{60}Co	^{137}Cs
1	21	1.85E+01	4.07E+00	1.87E+00	4.05E+00
2	21	1.31E+01	2.89E+00	1.33E+00	2.87E+00
5	20	8.42E+00	1.85E+00	8.50E-01	1.84E+00
10	20	6.09E+00	1.34E+00	6.15E-01	1.33E+00
15	20	5.09E+00	1.12E+00	5.14E-01	1.11E+00
20	20	4.50E+00	9.90E-01	4.54E-01	9.85E-01
50	20	3.18E+00	7.00E-01	3.21E-01	6.96E-01

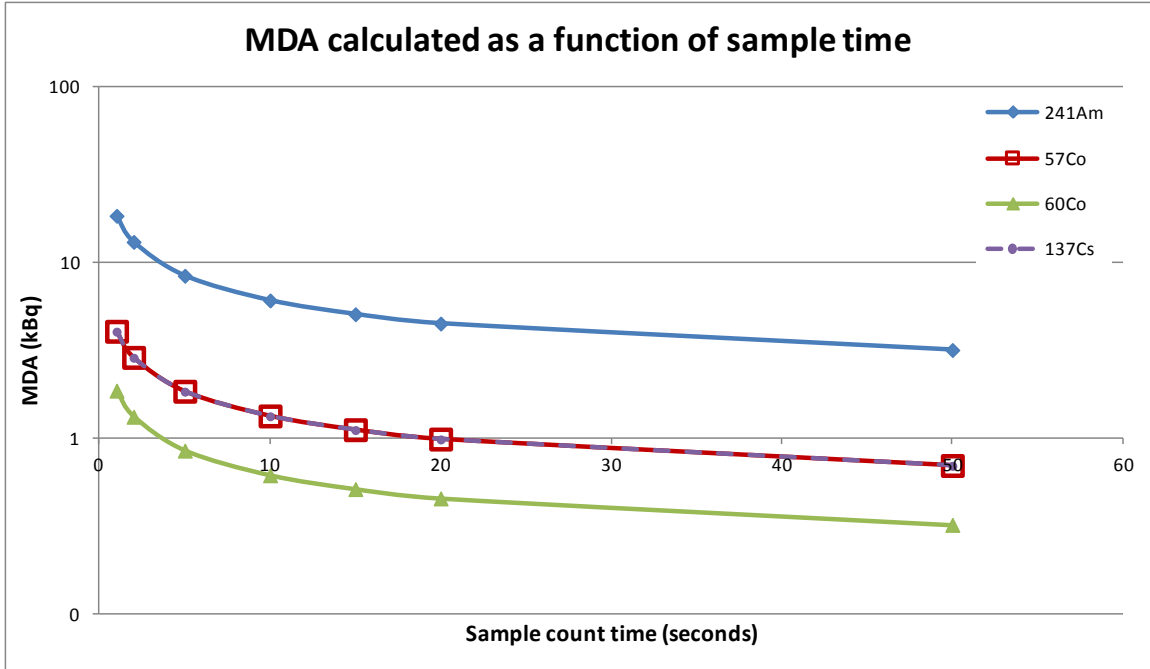


Figure 33: MDA as a function of sample time

The inhalation ALIs for the radioisotopes with a calculated MDA are provided in Table 13. They are taken from the RD-52 [31] except for ²⁴¹Am, not provided in the RD-52, which is taken from ICRP 68 [32] for a 5 µm AMAD and a type M (moderate) absorption rate. The MDAs from Figure 33 were converted into ALIs and plotted as a function of sample time in Figure 34.

Table 13: Annual Limits on Intake

Radioisotope	ALI (Bq)	DCF (Sv/Bq)
²⁴¹ Am	7.4E+02	2.7E-05
⁵⁷ Co	3.3E+07	6.0E-10
¹³⁷ Cs	3.0E+06	6.7E-09
⁶⁰ Co	1.2E+06	1.7E-08

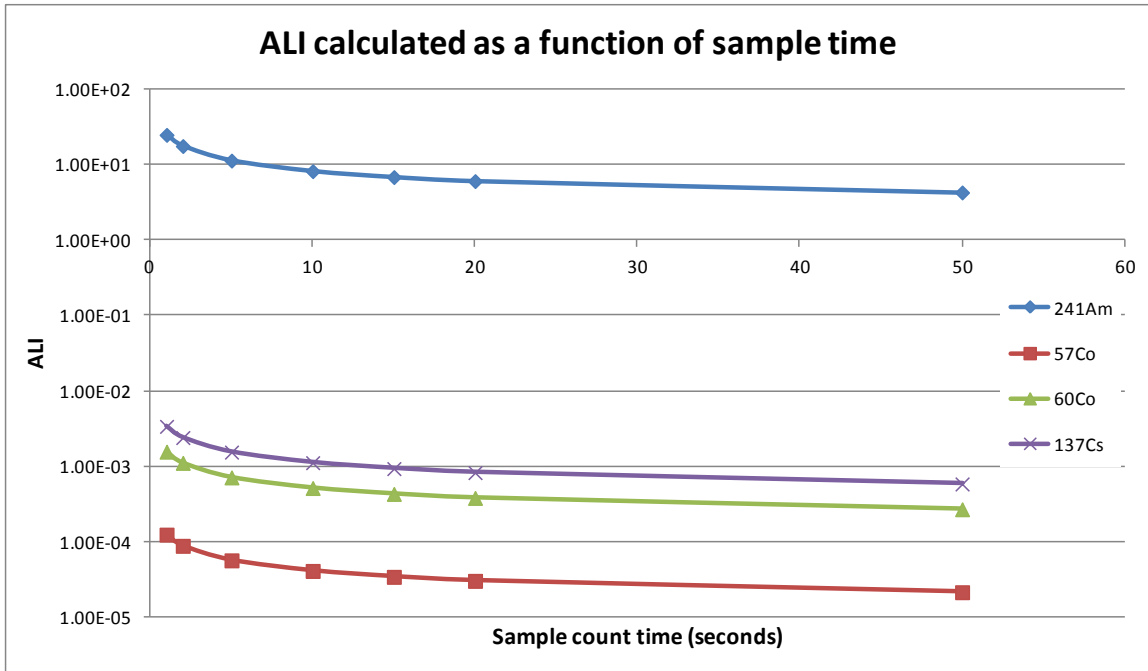


Figure 34: ALI as a function of sample time

The sample time required to measure 1/10 ALI is less than one second for ⁵⁷Co, ⁶⁰Co and ¹³⁷Cs. In fact, less than one second is sufficient to measure 1/100 ALI for these isotopes. A sample count time of 50 seconds is not enough to measure 1/10 ALI of ²⁴¹Am. This is due to the poor measurement efficiency for ²⁴¹Am coupled with its very high dose conversion factor (over five orders of magnitude larger than the DCF for ⁵⁷Co).

The results suggest that the PM12 is well suited for measuring internally deposited radioisotopes with gamma emissions above 100 keV. This is only true if the ALI of the radionuclide is sufficiently high (approximately above 10⁵ Bq). Applying this work to radioisotopes with gamma emissions below 100 keV or with low ALI values (less than 10⁵ Bq) should be done with caution. It was shown that the detection limit for ²⁴¹Am was not sufficient to measure 1/10 ALI in a reasonable period of time (< 50 seconds).

6. CONCLUSIONS AND RECCOMENDATIONS FOR FUTURE WORK

6.1 Conclusions

This research investigated the counting efficiency of the Thermo PM12 personnel portal monitor for the measurement of internal contamination localized to the lungs. A counting efficiency curve was calculated by Monte Carlo analysis using the Monte Carlo N Particle (MCNP) software. The counting efficiencies were used to calculate the minimum detectable activity for ^{241}Am , ^{57}Co , ^{60}Co and ^{137}Cs as a function of sample measurement time.

Three different computational phantoms were considered for this work: the adult male Bottle Mannequin Absorber (BOMAB) phantom, the University of Florida – Oak Ridge National Laboratories (UF-ORNL) stylized phantom, and the International Commission on Radiological Protection (ICRP) adult male voxel phantom provided by the Human Monitoring Laboratory (HML). The three phantoms increase in the approximation of anthropomorphicity in the order listed.

A bias ranging from 10-15% and 25-30% was observed at high energies (100-2000 keV) for the UF-ORNL and voxel computational phantoms respectively using the simulated counting efficiency for the BOMAB as a baseline. At low energies (< 100 keV) the bias dropped 20% (e.g., 10% to -10%) within a span of 60 keV for both the UF-ORNL and ICRP computational phantoms. This was attributed to the localization of the source distribution to the lungs of these phantoms whereas the source distribution is the entire chest cavity

for the BOMAB computational phantom. The particles originating in the lungs must travel through more tissue, allowing for attenuation, before exiting the body.

Benchmarking measurements of point sources and a BOMAB phantom were performed for the computational model of the PM12. The model was shown to respond accurately at high energies (<662 keV) with a 4-5% difference between measured and simulated values. The model responded poorly at lower energies (< 122 keV) with a difference of 33% between the measured and simulated values at 60 keV.

The measurement time required to measure 1/10 ALI of ^{41}Am , ^{57}Co , ^{60}Co and ^{137}Cs was estimated from the MDA calculations. It was discovered that a measurement time of less than one second was sufficient to measure less than 1/100 ALI of ^{57}Co , ^{60}Co and ^{137}Cs . A Measurement time of over 50 seconds was not sufficient to measure 1/10 ALI of ^{241}Am .

This work shows that the PM12 is well suited to measure internally deposited radionuclides with gamma emissions greater than 100 keV and with an ALI greater than 10^5 Bq with a short measurement time. Applying this work to radioisotopes with gamma emissions below 100 keV or with low ALI values (less than 10^5 Bq), such as ^{241}Am should be done with caution.

6.2 Recommendation for future work

The calculated MDAs are only applicable to source distributions in the lungs for the UF-ORNL and ICRP computational phantoms. The BOMAB results consider a source distributed throughout the chest cavity which could be extrapolated to other internal exposure scenarios such as an ingestion scenario.

Further work in this area could investigate the response of the PM12 to other source distributions. Accurate distributions of the source in the body could be modeled using software such as Dose and Risk Calculation (DCAL) released by the United States Environmental Protection Agency [77]. This software will calculate source distributions in body cavities for user selected radioisotopes as a function of time, radioactive decay, and anatomical parameters.

Many makes and models of portal monitors exist. The methodology for could be used to develop counting efficiency curves for other portal monitors.

REFERENCES

- [1] Kramer, G.H., K. Cappelo, B. Hauck, and J. Brown. Are Personnel Portal Monitors too Sensitive? *Radiation Protection Dosimetry* 127(1-4): 249-252; 2007.
- [2] Kramer, G.H., K. Capello, B.M. Hauck, J.T. Brown. Sensitivity of Portable Portal Monitors: Potential Problems when Dealing with Contaminated Persons. *Health Physics* 91(4):367-372; 2006.
- [3] International Atomic Energy Agency. *The Radiological Incident in Goiânia*. Vienna: IAEA; STI/PUB/815; ISBN 92-0-129088-8; 1988.
- [4] International Atomic Energy Agency. *IAEA safety Glossary: Terminology Used in Nuclear Safety and Radiation Protection*. Vienna: IAEA; STI/PUB/1290; 2007.
- [5] Berger, M.J., et al. *Stopping-Power and Range Tables for Electrons, Protons, and Helium Ions*. Visited: December 2014; <http://www.nist.gov/pml/data/star/>.
- [6] Canadian Nuclear Safety Commission. *Radiation Protection Regulations*. SOR/2000-203; Ottawa, Canada; 2014.
- [7] ANS. *Specifications for the Bottle Manikin Absorber Phantom*, ANSI/HPS, N13.35, 1999.
- [8] Kramer, G.H. and K. Capello, *The StandFast Whole Body Counter: Efficiency as a Function of BOMAB Phantom Size and Energy Modeled by MCNP 5*. *Health Physics* 92:290-296; 2007.

- [9] Kramer, G.H. and J. Fung. The FastScan whole body counter: Efficiency as a Function of BOMAB Phantom Size and Energy Modeled by MCNP. Proceedings of the 2004 International Congress on Radiation Protection, Madrid. Madrid: Spanish Society of Radiological Protection; 2004.
- [10] Kramer G.H., L.C. Burns, S. Guerriere. Monte Carlo Simulation of a Scanning Detector Whole Body Counter and the Effect of BOMAB Phantom Size on the Calibrations. Health Physics 83:526-533; 2002.
- [11] Kramer, G. H., Capello, K., and Phan, Q., NORMAN Phantom vs. the BOMAB Phantom: are they Different? Health Physics, 94(4): 355-361, 2008.
- [12] Dimbylow, P.J., FDTD Calculations of the Whole-body averaged SAR in an Anatomically Realistic Voxel Model of the Human Body from 1 MHz to 1 GHz. Physics in Medicine and Biology, 42, 479, 1997.
- [13] Jones, D.G. A Realistic Anthropomorphic Phantom for Calculating Organ Doses Arising from External Photon Irradiation. Radiation Protection Dosimetry, 72, 21, 2997.
- [14] Marinelli, L.D. Dosage determination with radioactive isotopes. Am. J. Roentgenol. Rad. Ther.: 47, 210, 1942.
- [15] Marinelli, L.D., E.H. Quimbly and G.J. Hine. Dosage determination with radioactive isotopes, II. Practical considerations in therapy and protection. Am. J. Roentgenol. Rad. Ther.: 59, 260, 1948.
- [16] Ellet, W.H., A.B. Callahan, and G.L. Borwnwell. Gamma-ray dosimetry of internal emitters, I. Monte Carlo calculations of absorbed doses from point

- sources. Brit. J. Radiol.: 37, 45, 1964.
- [17] Ellet, W.H., A.B. Callahan, and G.L. Brownwell. Gamma-ray dosimetry of internal emitters, II. Monte Carlo calculations of absorbed doses from uniform sources. Brit. J. Radiol.: 38, 541, 1965.
- [18] Reddy A.R., W.H. Ellet, and G.L. Brownwell. Gamma-ray dosimetry of internal emitters, I. Monte Carlo calculations of absorbed doses for low-energy gamma-rays. Brit. J. Radiol.: 42, 512, 1967.
- [19] Xu, X.G and Eckerman, K.F., Handbook of Anatomical Models for Radiation Dosimetry. Boca Raton: CRC Press, 2010. Print.
- [20] Fisher, H.J.L., and Snyder, W.S., Variation of Dose Delivered by ¹³⁷Cs as a Function of Body Size from Infancy to Adulthood. ORNL-4007, Oak Ridge, TN: ORNL, p. 211, 1966
- [21] Fisher, H.J.L., and Snyder, W.S., Distribution of Dose in the Body from a Source of Gamma Rays Distributed Uniformly in an Organ, ORNL-4168, Oak Ridge, TN: ORNL, p. 245, 1967.
- [22] Bush, F. The integral dose received from a uniformly distributed radioactive isotope. British J Radiol. 22:96-102; 1949.
- [23] Kramer, G., Burns, L., and Noel, L., The BRMD BOMAB Phantom Family. Health Physics, 61(6): 895-902, 1991.
- [24] ICRP, Report of the Task Group on Reference Man, ICRP Publication 23, Pergamon Press, Oxford, 1975.
- [25] Knoll, G.F. Radiation detection and Measurement, third edition. John Wiley & Sons, 2000.

- [26] Evans, R.D. *The Atomic Nucleus*. McGraw-Hill Book Company, 1955.
- [27] Rake, K.D. Evaluating the response of Polyvinyl Toluene Scintillators used in Portal Detectors. M.Sc. thesis, Air Force Institute of Technology, USA.
- [28] Los Alamos National Laboratory X-5 Monte Carlo Team. MCNP – A General Monte Carlo N-Particle Transport Code, Version 5. Volume I: Overview and Theory. 24 April, 2003 (Revised 2/1/2008).
- [29] Kramer, G.H., K. Capello, and J. Sung. The LLNL voxel phantom: comparison with the physical phantom and previous virtual phantoms. *Health Physics* 93(6):696-700; 2007.
- [30] International Atomic Energy Agency. International basic safety standards for protection against ionizing radiation and for the safety of radiation sources. Safety series No. 115; Vienna: 2005.
- [31] Canadian Nuclear Safety Commission. RD-52: Design guide for nuclear substance laboratories and nuclear medicine rooms. DRAFT. Ottawa: 2008.
- [32] ICRP, 1994. Dose Coefficients for Intakes of Radionuclides by Workers. ICRP Publication 68. *Ann. ICRP* 24 (4).
- [33] Hurtado, J.L., et. al. Hybrid Computational Phantoms Representing the Reference Adult Male and Adult Female: Construction and Applications for Retrospective Dosimetry. *Health Physics* 102(3): 292-304; 2012.
- [34] Loevinger, R. and M. Berman. MIRD Pamphlet No.1: A schema for absorbed dose calculations for Biologically Distributed Radionuclides. New York: Society of Nuclear Medicine; 1968.

- [35] Berger, M.J. MIRDPamphlet No.2: Energy Deposition in Water by Photons from Point Isotropic Sources. New York: Society of Nuclear Medicine; 1968.
- [36] Brownell, G.L., W.H. Ellett and A.R. Reddy. MIRDPamphlet No.3: Absorbed Fractions for Photon Dosimetry. New York: Society of Nuclear Medicine; 1968.
- [37] Snyder, W.S., et. al. Estimates of absorbed fractions for monoenergetic photon sources uniformly distributed in various organs of a heterogeneous phantom. J Nucl Med, 10 (Suppl. 3), 7 1969.
- [38] Snyder, W.S., M.R. Ford and G.G. Warner. MIRDPamphlet No. 5, Revised Estimates of Specific Absorbed Fractions for Monoenergetic Photon Sources Uniformly Distributed in Various Organs of a Heterogeneous Phantom. New York: Society of Nuclear Medicine, 1978.
- [39] Zubal, I.G., Harrell, C.R, Smith, E.O, Rattner, Z., Gindi, G. and Hoffer, P.B., Computerized three-dimensional segmented human anatomy, Medical Physics, 21(2): 299-302, 1994.
- [40] Jones, D.G. A Realistic Anthropomorphic Phantom for Calculating Organ Doses Arising from External Photon Irradiation. Radiation Protection Dosimetry, 72(1): 21-29, 1997.
- [41] Yale Image Processing and Analysis Group. The Zubal phantom. Visited: November 2014; <http://noodle.med.yale.edu/zubal/>.
- [42] Wikipedia. Non-uniform rational B-spline. Visited: November 2014; http://en.wikipedia.org/wiki/Non-uniform_rational_B-spline.

- [43] W. P. Segars. Development of a New Dynamic NURBS-based Cardiac-torso (NCAT) Phantom. Ph.D. dissertation, Univ. of North Carolina, Chapel Hill, May 2001.
- [44] U.S. National Laboratory of Medicine. The Visible Human Project. Visited: November 2014;
http://www.nlm.nih.gov/research/visible/getting_data.html#.
- [45] Segars, W. and B. Tsui. 4D MOBY and NCAT Phantoms for Medical Imaging Simulation of Mice and Men. J Nucl Med Meet Abst; 48: 203; 2007.
- [46] W. P. Segars, T. S. Lee, and B. M. W. Tsui, B. Simulation of Motion Defects in the 4D NCAT Cardiac Model, J. Nucl. Med 44(5): 142, 2003.
- [47] Wikipedia. Computational Human Phantom. Visited: November 2014;
http://en.wikipedia.org/wiki/Computational_human_phantom.
- [48] E. Han, W. E. Bolch, and K. F. Eckerman. Revisions to the ORNL Series of Adult and Pediatric Computational Phantoms for Use with the MIRD Schema. Health Physics; 90(4): 337–356, 2006.
- [49] ICRP, 2002. Basic Anatomical and Physiological Data for Use in Radiological Protection Reference Values. ICRP Publication 89. Ann. ICRP 32 (3-4).
- [50] ICRP, 2009. Adult Reference Computational Phantoms. ICRP Publication 110. Ann. ICRP 39 (2).
- [51] Han, E. Revised Series of Stylized Anthropometric Phantoms for Internal and External Dose Assessment". Ph.D Dissertation, University of Florida,

2005.

- [52] Tremblay, M., G.H. Kramer, K. Capello, and P. Segars. Effect of Respiratory Motion on Lung Counting Efficiency using a 4D NURBS-based Cardio-torso (NCAT) Phantom. *Health Physics* 109(6): 564-569; 2014.
- [53] Los Alamos National Laboratory X-5 Monte Carlo Team. MCNP – A General Monte Carlo N-Particle Transport Code, Version 5. Volume 2: User's Guide. 24 April, 2003 (Revised 10/03/2005, 2/1/2008).
- [54] Kawrakow, I., et al. The EGSnrc Code System: Monte Carlo Simulation of Electron and Photon Transport. NRCC Report: PIRS-701; 31 March, 2013.
- [55] GEANT4. GEANT4 User Documentation. Last updated: 12/07/2013; <http://geant4.cern.ch/support/userdocuments.shtml>.
- [56] Nuclear Energy Agency. PENELOPE2011. Visited: November 2014; <http://www.oecd-nea.org/tools/abstract/detail/nea-1525>.
- [57] FLUKA team. FLUKA. Visited: November 2014; <http://www.fluka.org/fluka.php>.
- [58] Capello, K., S. Kedzior, and G.H. Kramer. Voxel Phantoms: the New ICRP Computational Phantoms: How do they Compare? *Health Physics* 102(6): 626-630, June 2012.
- [59] Akkurt, H., K.F. Eckerman. Development of PIMAL: Mathematical Phantom with Moving Arms and Legs. Oak Ridge National Laboratory: May 2007.

- [60] White Rock Science. Moritz Geometry Tool. Visited: November 2014;
<http://www.whiterockscience.com/moritz.html>.
- [61] Schwarz, A. L., R. A. Schwarz, and L. L. Carter. MCNP/MCNPX Visual Editor Computer Code Manual for Vised Version 22S. February 2008.
- [62] Visual Editor Consultants. MCNP Vised. Visited: November 2014;
<http://www.mcnpvised.com/company/company.html>.
- [63] CANUS Plastics Inc. Phantoms. Report HMLT-90-I.
- [64] Kinectrics. Technical Memorandum: K-973912-1280-TM-OPGHP-PM1-R0. May, 2012.
- [65] National Nuclear Data Center. Decay Radiation Database. Last updated: 07/14/2014; http://www.nndc.bnl.gov/nudat2/indx_dec.jsp
- [66] Thermo Fisher Scientific. Manual-PM12. Berkshire, UK: February 5, 2008.
- [67] International Electrotechnical Commission. "International Standard IEC 61098: Radiation protection instrumentation – installed personnel surface contamination monitoring assemblies. Second edition; Geneva, Switzerland: 2003.
- [68] Thermo Scientific. PM12 Personnel Gamma Portal Monitor – Thermo Scientific. Visited: 20 April 2011.
<http://www.thermoscientific.com/ecom/servlet/productsdetail_11152_L10447_81900_11961362_-1 >
- [69] Thermo Scientific. PM12 – Personnel Gamma Portal Monitor. Manufacturer specification sheet; Issued: 2009.

- [70] Thermo Scientific. Additional features of PM12 compared to PM7. Manufacturer information brochure; Issued: unknown date.
- [71] Thermo Scientific. Frequently Asked Questions – PM12 Gamma Portal Monitor. Manufacturer information brochure; Issued: 1 April 2009.
- [72] Berger, M.J., et al. XCOM: photon cross section database. Visited: December 2014; <http://www.nist.gov/pml/data/xcom/>.
- [73] Bicron. BC-400/BC-404/BC-408/BC-412/C-416 Premium Plastic Scintillators. Manufacturer specification sheet; Issued: unknown date.
- [74] AZO Materials. Stainless Steel – Grade 446. Visited: February 2014; <http://www.azom.com/article.aspx?ArticleID=6817>.
- [75] University of Columbia Department of Earth and Environmental Sciences. Gaseous Composition of Dry Air. Visited: February 2014; http://eesc.columbia.edu/courses/ees/slides/climate/table_1.html.
- [76] Kramer, G.H. P. Crowley and L.C. Burns. The Uncertainty in the Activity Estimate from a Lung Counter Due to the Variability in Chest Wall Thickness Profile. Health Physics 78(6): 739-743; 2000.
- [77] Eckerman, K.F., et. al. User's Guide to the DCAL System. ORNL/TM-2001/190; 2006.

ANNEX A. BOMAB FILL SOLUTION CALIBRATION REPORT

TECHNICAL MEMORANDUM: K-973912-1280-TM-OPGHP-PM1-R0

May 2nd, 2012

Mr. Daniel Oancea
 Senior Scientist
 Dosimetry Section, Health Physics Department
 Phone: 905 430 2215 ext 3363
 e-mail: daniel.oancea@opg.com

OPG PO# 00214528-0003

Subject: Activity of Radionuclides in the 2012 WBC Phantom

Isotope	Expected Activity (Bq)			Observed (Bq)
K-40	6000	±	300	5985
Co-57*	5010	±	250	4910
Co-60*	3510	±	180	3585
Cs-137*	4500	±	200	4590

*Reference date for decay correction is 4-April-2012

Prepared by:

Reviewed by:

Approved by:

--signed--

--signed--

--signed--

Reid Mowat
 Senior Technologist
 Analytical and Waste Services

Robert Taylor
 Scientist
 Analytical and Waste Services

Otto Herrmann
 Department Manager
 Analytical and Waste Services

The Analytical and Environmental Laboratory of Kinectrics is certified by the Standards Council of Canada as conforming with ISO 17025. All methods and procedures adhere to strict guidelines and quality control protocols.

Kinectrics Inc has prepared this memorandum in accordance with and subject to the Master Services Agreement between Kinectrics Inc. and Ontario Power Generation Inc, dated June 30th, 2009.

© Kinectrics Inc., 2012

Analytical and Waste Services, Generation Life Cycle Management
 Location: KJ-135; Phone: (416) 207-6000 - Ext. 6045; FAX # (416) 207-5550

ANNEX B. GAMMA RAY EMISSION ENERGIES AND YIELDS

Radioisotope	Gamma energy (keV)	Gamma yield (%)
²⁴¹ Am	26.3446	2.27
	33.196	0.126
	59.5409	35.9
⁵⁷ Co	122.0614	85.60
	136.4743	10.68
	692.03	0.157
⁶⁰ Co	1173.237	99.9736
	1332.501	99.9856
¹³⁷ Cs	661.657	85.1
⁴⁰ K	1460	10.66

ANNEX C. BENCHMARKING MEASUREMENTS DATA

Note that the measurement data for the centroid efficiency, individual PVT measurements and the BOMAB phantoms measurements are background subtracted.

Experiment	Source	Time (s)	Detector 1 (cps)	Detector 2 (cps)	Detector 3 (cps)	Detector 4 (cps)	Detector 5 (cps)	Detector 6 (cps)	Detector 7 (cps)	Detector 8 (cps)	Sum (cps)	error (+/- cps)
Background measurements	None	100	803.2	711.5	672.9	635.5	648.5	654.8	626.9	798.2	5551.5	7.5
Centroid efficiency	¹³⁷ Cs	100	89.5	205.8	201.8	547.9	570.6	241	242.6	115.4	2214.6	11.6
	⁶⁰ Co	100	57.8	141.7	125.7	332.3	370	145.9	165.4	77	1415.8	11.2
	²⁴¹ Am	100	0	11.6	2.1	54.4	56.5	17.2	22.3	10.7	173.5	10.7
Individual PVT measurements	¹³⁷ Cs	50	5690.2	6162.5	5982.1	5828.5	5790.3	5833.2	5945.8	5948.1	N/A	N/A
	⁶⁰ Co	50	3732.4	3935.5	3814	3631.8	3740.4	3662.2	3753.2	2775.5	N/A	N/A
	²⁴¹ Am	50	5.8	651.3	537.9	543.3	577.3	683.5	570.5	529	N/A	N/A
BOMAB phantom measurements	Mixture	100	32.5	118.9	111.3	205	208.3	169.3	161.6	130	1136.9	11.1

ANNEX D. SIMULATION DATA

Results of the centroid efficiency simulations

Detector	⁵⁷ Co		⁶⁰ Co		¹³⁷ Cs		²⁴¹ Am	
	Response	Error	Response	Error	Response	Error	Response	Error
1	4.72E-03	3.26E-02	5.81E-03	1.88E-02	6.87E-03	1.20E-03	1.16E-04	9.30E-03
2	3.01E-02	1.44E-02	2.27E-02	8.45E-03	2.89E-02	6.00E-04	2.93E-03	1.80E-03
3	4.72E-03	3.10E-02	5.81E-03	1.64E-02	6.88E-03	1.20E-03	1.16E-04	9.30E-03
4	4.73E-03	3.26E-02	5.82E-03	1.78E-02	6.88E-03	1.20E-03	1.17E-04	9.20E-03
5	3.01E-02	1.42E-02	2.27E-02	8.50E-03	2.89E-02	6.00E-04	2.93E-03	1.80E-03
6	4.72E-03	3.16E-02	5.82E-03	1.76E-02	6.87E-03	1.20E-03	1.18E-04	9.20E-03
7	5.24E-03	3.69E-02	4.14E-03	1.98E-02	5.31E-03	1.40E-03	5.69E-04	4.20E-03
8	5.23E-03	3.77E-02	4.14E-03	2.08E-02	5.29E-03	1.40E-03	5.63E-04	4.20E-03
Total	8.96E-02	1.07E-02	7.69E-02	5.89E-03	9.60E-02	4.03E-04	7.45E-03	2.45E-03

Results of the efficiency curve simulations

Phantom	detector	Response at photon energy						
		60 keV	122 keV	279 keV	662 keV	1173 keV	1332 keV	2000 keV
BOMAB MCNP5	bottom r	3.76E-04	8.31E-04	1.22E-03	1.49E-03	1.65E-03	1.69E-03	1.80E-03
	mid r	1.17E-02	1.97E-02	2.30E-02	2.20E-02	2.02E-02	1.97E-02	1.83E-02
	top r	5.46E-03	9.17E-03	1.06E-02	1.01E-02	9.36E-03	9.18E-03	8.57E-03
	bottom l	3.88E-04	8.22E-04	1.21E-03	1.48E-03	1.65E-03	1.68E-03	1.79E-03
	mid l	1.14E-02	1.93E-02	2.26E-02	2.17E-02	2.00E-02	1.96E-02	1.82E-02
	top l	5.41E-03	9.06E-03	1.05E-02	1.00E-02	9.29E-03	9.08E-03	8.47E-03
	foot	1.68E-04	3.71E-04	5.03E-04	5.61E-04	5.84E-04	5.92E-04	6.23E-04
	ceiling	1.83E-03	3.13E-03	3.65E-03	3.55E-03	3.37E-03	3.34E-03	3.24E-03
	sum	3.68E-02	6.23E-02	7.32E-02	7.10E-02	6.61E-02	6.49E-02	6.09E-02
UF-ORNL MCNP5	bottom r	1.78E-04	4.91E-04	7.49E-04	9.90E-04	1.18E-03	1.24E-03	1.38E-03
	mid r	5.94E-03	1.22E-02	1.50E-02	1.51E-02	1.44E-02	1.42E-02	1.34E-02
	top r	8.24E-03	1.68E-02	2.00E-02	1.95E-02	1.80E-02	1.76E-02	1.64E-02
	bottom l	1.98E-04	5.28E-04	7.81E-04	1.04E-03	1.23E-03	1.28E-03	1.44E-03
	mid l	6.73E-03	1.35E-02	1.62E-02	1.62E-02	1.53E-02	1.50E-02	1.42E-02
	top l	8.98E-03	1.81E-02	2.13E-02	2.05E-02	1.90E-02	1.85E-02	1.71E-02
	foot	9.53E-05	2.37E-04	2.94E-04	3.08E-04	3.25E-04	3.29E-04	3.67E-04
	ceiling	3.01E-03	5.74E-03	6.69E-03	6.51E-03	6.12E-03	5.99E-03	5.62E-03
	sum	3.34E-02	6.75E-02	8.10E-02	8.03E-02	7.56E-02	7.42E-02	7.00E-02

MIRD MCNPX	bottom r	1.80E-04	4.98E-04	7.39E-04	9.85E-04	1.18E-03	1.24E-03	1.37E-03
	mid r	5.95E-03	1.22E-02	1.50E-02	1.51E-02	1.44E-02	1.42E-02	1.34E-02
	top r	8.26E-03	1.68E-02	2.00E-02	1.95E-02	1.80E-02	1.76E-02	1.64E-02
	bottom l	1.98E-04	5.27E-04	7.83E-04	1.04E-03	1.24E-03	1.29E-03	1.43E-03
	mid l	6.72E-03	1.35E-02	1.63E-02	1.63E-02	1.54E-02	1.51E-02	1.42E-02
	top l	9.00E-03	1.80E-02	2.13E-02	2.05E-02	1.90E-02	1.85E-02	1.71E-02
	foot	9.94E-05	2.36E-04	2.97E-04	3.05E-04	3.32E-04	3.38E-04	3.71E-04
	ceiling	3.01E-03	5.75E-03	6.70E-03	6.53E-03	6.11E-03	5.98E-03	5.63E-03
	sum	3.34E-02	6.75E-02	8.10E-02	8.03E-02	7.56E-02	7.42E-02	7.00E-02
VOXEL MCNPX	bottom r	3.25E-04	8.78E-04	1.27E-03	1.57E-03	1.75E-03	1.78E-03	1.86E-03
	mid r	8.46E-03	1.63E-02	1.90E-02	1.83E-02	1.68E-02	1.64E-02	1.53E-02
	top r	1.17E-02	2.32E-02	2.67E-02	2.50E-02	2.24E-02	2.18E-02	1.99E-02
	bottom l	2.25E-04	6.58E-04	9.70E-04	1.22E-03	1.37E-03	1.41E-03	1.52E-03
	mid l	6.51E-03	1.33E-02	1.61E-02	1.59E-02	1.49E-02	1.46E-02	1.37E-02
	top l	1.00E-02	2.04E-02	2.37E-02	2.25E-02	2.04E-02	1.99E-02	1.82E-02
	foot	9.67E-05	2.60E-04	3.60E-04	3.78E-04	3.90E-04	3.99E-04	4.16E-04
	ceiling	3.08E-03	6.34E-03	7.45E-03	7.12E-03	6.57E-03	6.45E-03	6.06E-03
	sum	4.05E-02	8.14E-02	9.56E-02	9.20E-02	8.46E-02	8.27E-02	7.69E-02

ANNEX E. MCNP INPUT CARD

PM12 centroid efficiency simulation

c

c -CELL CARDS-

c

c Portal monitor cells

c

```
21 7 -2.7 -21 22 -23 25 -29 210 imp:p=1 $ floor plate
22 4 -7.8 27 -28 -23 25 -29 210 imp:p=1 $ ceiling plate
23 7 -2.7 23 -24 -28 21 -29 210 imp:p=1 $ passage wall
24 7 -2.7 -25 26 -28 21 -29 210 imp:p=1 $ passage wall
31 6 -1.032 31 -32 37 -39 -313 314 imp:p=1 $ bottom r detector
32 6 -1.032 33 -34 37 -39 -313 314 imp:p=1 $ mid r detector
33 6 -1.032 35 -36 37 -39 -313 314 imp:p=1 $ top r detector
34 6 -1.032 31 -32 -38 310 -313 314 imp:p=1 $ bottom l detector
35 6 -1.032 33 -34 -38 310 -313 314 imp:p=1 $ mid l detector
36 6 -1.032 35 -36 -38 310 -313 314 imp:p=1 $ top l detector
37 6 -1.032 -315 316 -321 322 -313 314 imp:p=1 $ foot detector
38 6 -1.032 -319 318 -321 322 -313 314 imp:p=1 $ ceiling detector
39 5 -11.34 31 -32 39 -311 -313 314 imp:p=1 $ bottom r lead
310 5 -11.34 33 -34 39 -311 -313 314 imp:p=1 $ mid r lead
311 5 -11.34 35 -36 39 -311 -313 314 imp:p=1 $ top r lead
312 5 -11.34 31 -32 -310 312 -313 314 imp:p=1 $ bottom l lead
313 5 -11.34 33 -34 -310 312 -313 314 imp:p=1 $ mid l lead
314 5 -11.34 35 -36 -310 312 -313 314 imp:p=1 $ top l lead
315 5 -11.34 -316 317 -321 322 -313 314 imp:p=1 $ foot lead
316 5 -11.34 -320 319 -321 322 -313 314 imp:p=1 $ ceiling lead
```

c

c Universe cells

c

```
66 1 -0.00129 -666 #21 #22 #23 #24 #31 #32 #33 #34 #35 #36 #37 #38 #39
    #310 #311 #312 #313 #314 #315 #316 imp:p=1
62 0 666 imp:p=0 $ kill particles
```

c

c Blank line

c

c -SURFACE CARDS-

c

c Portal monitor surfaces

c

```
21 pz 0 $ passage floor
```

22 pz -0.4 \$ passage floor Al
 23 py 35.5 \$ passage wall
 24 py 35.9 \$ passage wall Al
 25 py -35.5 \$ passage wall
 26 py -35.9 \$ passage wall Al
 27 pz 204 \$ passage ceiling
 28 pz 204.4 \$ passage ceiling Fe
 29 px 30.5 \$ PM edge
 210 px -30.5 \$ PM edge
 31 pz 16 \$ bottom low detector
 32 pz 72 \$ top low detector
 33 pz 74 \$ bottom mid detector
 34 pz 130 \$ top mid detector
 35 pz 132 \$ bottom high detector
 36 pz 188 \$ top high detector
 37 py 36 \$ detector face
 38 py -36 \$ detector face
 39 py 41 \$ detector back
 310 py -41 \$ detector back
 311 py 42.25 \$ Pb shield back
 312 py -42.25 \$ Pb shield back
 313 px 15.5 \$ detector side
 314 px -15.5 \$ detector side
 315 pz -0.5 \$ top foot detector
 316 pz -5.5 \$ bottom foot detector
 317 pz -6.75 \$ bottom lead shielding
 318 pz 204.5 \$ bottom ceiling detector
 319 pz 209.5 \$ top ceiling detector
 320 pz 210.75 \$ top lead shielding
 321 py 28 \$ detector side
 322 py -28 \$ detector side
 c 323 pz 15.9
 c 324 pz 72.1
 c 325 pz 73.9
 c 326 pz 130.1
 c 327 pz 131.9
 c 328 pz 188.1
 c 329 py 35.9
 c 330 py -35.9
 c 331 px 15.6
 c 332 px -15.6
 c
 c Outer universe
 666 so 500 \$ 5 metre sphere
 c
 c Blank line

```

c
c -MISC CARDS-
c
mode p
c -MATERIALS CARDS-
c
c AIR
m1 7000.      0.78
    8000.      0.21
    18000.     0.01
c
c STAINLESS STEEL
m4 26000 -0.73 24000 -0.27
c
c LEAD
m5 82000.     1
c
c POLYVINYL TOLUENE (PVT) SCINTILLATOR
m6 1000.      1.104 $ ratio of H to C atoms
    6000.      1
c
c ALUMINIUM
m7 13000.     1
c
c -SOURCE CARDS-
c
sdef erg=d1 par=2 pos=0 0 102
si1 | 0.1220614 0.1364743 0.69203
sp1 0.856 0.1068 0.00157
sb1 1 2R
f8:p 31 32 33 34 35 36 37 38
E8 0 1E-5 0.662 0.700 1.300 10
nps 10000000
mode p
print 10 20 30 126

```